Volumetric measurement of turbulence and flow topology in an asymmetric diffuser

Prashant Das and Sina Ghaemi*
Department of Mechanical Engineering, University of Alberta, Edmonton, Alberta T6G 1H9, Canada

(Received 5 March 2020; accepted 23 October 2020; published 13 November 2020)

The turbulent flow in a three-dimensional asymmetric diffuser was experimentally investigated using time-resolved, three-dimensional particle tracking velocimetry (3D-PTV). The diffuser geometry chosen for this study was a benchmark geometry devised and studied experimentally by Cherry *et al.* [Intl. J. Heat Fluid Flow 29, 3 (2008)], with a few subsequent numerical simulations at a Reynolds number of 10 000. In the present paper, we applied a state-of-the-art 3D-PTV to measure the 3D structure of the flow field in the entire diffuser for five Reynolds numbers (Re), ranging from 9200 up to 29 400. We found that the mean velocity fields were qualitatively similar across all Re studied. The volumetric fraction of the backflow region, when quantified using an intermittency factor of $\gamma < 0.8$, was in the range of 11–14%, with a marginal decrease with increasing Re. The maximum values of normal and shear Reynolds stresses were located in the regions close to the edge of the backflow region, and the peak values for the streamwise normal Reynolds stress increased with Re. The corner vortices, which formed in the channel preceding the diffuser, showed the existence of secondary flow well within the diffuser region. The strength of these vortices reduced with increasing Re. A modal decomposition of the turbulent fluctuations using spectral proper orthogonal decomposition (SPOD) showed large-scale structures in the flow. The SPOD analysis revealed that these large-scale structures were associated with low frequency oscillations in the band of St = [0.003 0.03], with two frequency peaks at St = 0.012 and 0.028. The three-dimensional separation along the two diverging walls of the diffuser was characterized by detecting critical points in the near-wall streamlines. These critical points were investigated in relation to three large-scale vortical structures identified within the diffuser. The flow topology in the diffuser showed that two of these vortical structures originated from the wall with the largest diverging angle and were connected by a separation surface. The third vortical structure originated from the neighboring diverging wall and was bound by another large separation surface.

DOI: 10.1103/PhysRevFluids.5.114605

I. INTRODUCTION

In many practical wall-bounded turbulent flows, separation is a phenomenon that occurs when there are sudden changes in the geometry (a sharp edge as in a backward-facing step) or when there is an adverse pressure gradient (due to a gradual increase in the cross-sectional area of a duct, for example). While in the former case it is rather intuitive to predict the location of separation, it becomes more challenging to predict the separation location in the case of separation induced by an adverse pressure gradient. This is primarily because of its three-dimensionality and sensitivity to flow parameters such as pressure gradient, turbulence levels, and boundary conditions [1].

*ghaemi@ualberta.ca

Most initial studies on turbulent separation focused on flows that had a two-dimensional (2D) mean velocity field, at least in a limited region at the midspan of the flow field [2]. This was primarily owing to the simplicity it offers in characterizing the flow field and identifying the factors contributing to flow separation. However, it has since been established that the canonical 2D flows studied in a laboratory are not truly 2D because of the finite lateral dimension that can introduce three-dimensional (3D) disturbances. This, for example, was shown to be the case in the experiments of Obi *et al*. [3] with plane diffusers which had only one diverging wall. Further investigation of such plane diffusers by Buice and Eaton [4], showed that end-wall effects could prevent the flow from being truly 2D. Kaltenbach [5] used large eddy simulations to study such diffusers and observed a three-dimensional mean flow. Similar observations related to the three-dimensionality of the flow have also been made for flows past a backward-facing step, even at large aspect ratios where two-dimensionality is expected [6].

The diffuser geometry, where fluid passes through a confined duct or pipe with increasing cross-sectional area, finds relevance in many industrial applications. Numerous investigations, both experimental and computational, have been carried out on such a configuration to characterize flow separation [3,4,7–12]. Cherry *et al*. [9] developed an idealized diffuser geometry to study 3D turbulent separation. Specifically, this geometry was designed to avoid symmetry and involved a rectangular diffuser with two adjacent walls diverging at different angles. The main motivation behind this experimental study was to create a benchmark for the evaluation of future numerical simulations [11,13–15]. Cherry *et al*. [9] conducted 3D velocity measurements within the diffuser at a Reynolds number of approximately 10 000 using magnetic resonance velocimetry. They presented the mean flow field in the diffuser region, showing that the flow separated first from the corner joining the two diverging walls. Additionally, they showed that the peak of the root mean square of streamwise velocity fluctuations reached up to 20% of the bulk inlet velocity. The effect of geometrical sensitivity on the flow was also explored by investigating a second asymmetric diffuser with slightly different diverging angles. Subsequent direct numerical simulation (DNS) by Ohlsson *et al*. [11] on one of the diffuser geometries (henceforth referred to as diffuser 1 after Cherry *et al*. [9]) showed good agreement in terms of the mean flow characteristics and the area fraction of the separated region in the diffuser. Numerical simulations on the same diffuser geometry later showed that the separation behavior in the diffuser was very sensitive to the inlet conditions, most notably the secondary flows [11,13,14]. Grundmann *et al*. [16,17] used plasma actuators and vortex generators to manipulate the inlet flow preceding the diffuser. They showed through direct pressure measurements, that the pressure recovery of the diffuser could be altered significantly by making small changes to the inlet flow. Sayles and Eaton [18] showed using planar particle image velocimetry (PIV) measurements that inlet flow perturbations caused the separation bubble's size and orientation to change.

Malm *et al*. [15] carried out a detailed study of diffuser 1 using DNS and extended the analysis to include frequency information using time probes in the separated region. They reported the persistence of a weak secondary flow, which developed in the upstream channel and extended into the diffuser section. Furthermore, they identified coherent structures using proper orthogonal decomposition (POD) of the turbulent flow and showed the presence of large streaks in the diffuser. However, the POD analysis did not identify any energy dominant mode. Overall, the DNS results highlighted the presence of large-scale, low-frequency, quasiperiodic flow in the 3D diffuser [15]. This low-frequency periodicity was attributed to flow confinement in this geometry and was compared with similar observations made in studies involving jet flows confined within a rectangular cavity [19]. However, these investigations have not yet been substantiated with experimental data because of the absence of time-resolved information in the measurements of Cherry *et al*. [9].

To identify the origin and topology of such 3D separation, the pattern of skin-friction lines on the diverging walls of the diffuser should also be investigated. Délery [20] showed that complex 3D separation can be characterized by identifying the critical points of skin-friction lines. This idea has indeed been extensively used in the past to identify separation regions on bluff bodies using surface flow visualization [21]. More recently, near-wall planar PIV has been used to extract streamlines

close to the walls in both external [22] and internal [23] flows. With a near-wall description of separation using skin-friction lines, we can then relate the separation process to any large-scale structures within the flow.

The objective of the present paper is to carry out a detailed experimental investigation of the turbulent flow field in diffuser 1 of Cherry *et al*. [9]. We study five different Re between approximately 9200 and 29 400. We systematically present results characterizing the 3D separation by studying both the mean flow field and the instantaneous flow features. To achieve the present objectives, we conduct 3D velocity measurements in the entire diffuser using time-resolved 3D particle tracking velocimetry (3D-PTV). The shake-the-box (STB) algorithm [24–26] is used to extract the Lagrangian particle tracks. This state-of-the-art algorithm can provide temporal consistency of small scale structures while maintaining a high spatial resolution [25]. To better understand the topological aspects, we investigate the in-plane streamlines in the vicinity of the diverging walls, and study them in relation to the large-scale flow structures. In addition to 3D-PTV in the present paper, two-component, time-resolved PIV measurements are also conducted in the straight channel section preceding the diffuser to verify the fully developed state of the inlet flow.

The outline of the paper is as follows. In Sec. II, we present the details of the experimental setup and the 3D-PTV measurement technique. The experimental results are presented in the subsequent sections, starting with a characterization of the diffuser inlet in Sec. III. Results from the mean flow analysis are presented in Sec. IV. Further analysis of the large-scale structures observed in the flow using spectral POD and skin-friction lines are presented in Sec. V. Finally, the conclusions drawn from this study are presented in Sec. VI.

II. EXPERIMENTAL PROCEDURE

A schematic of the diffuser is shown in Fig. 1. The diffuser consists of two diverging walls referred to here as wall 1 and wall 2 with diverging angles of 11.30° and 2.56°, respectively. The coordinate system along with the origin adopted in the present paper is also shown in Fig. 1(b). Further details on the experimental setup and measurement techniques are presented below.

A. Flow setup

The experiments were carried out in a closed-circuit flow loop using water as the working fluid. The setup utilized a progressing cavity pump (Moyno 36704) with a 2 HP motor which was controlled using a variable-frequency drive (VFD). The frequency setting of the VFD determined the pump RPM and consequently the flow rate through the loop. The flow loop consisted of circular PVC pipes with 50-mm diameter, which connected the reservoir to the pump and the pump to the inlet section shown in the left side of Fig. 2. The components shown in Fig. 2 are labeled using letters A through H. The inlet section (A–D) consisted of a diverging duct (A and B) which connected to a settling chamber (B and C), both having a circular cross section. The settling chamber consisted of a honeycomb mesh to ensure a uniform flow. The flow then passed through a converging duct (C and D) which was 3D printed to smoothly transition the circular cross section on one end to a rectangular cross section on the other. The nozzle had a contraction ratio of 18.6 and its converging end was connected to an acrylic rectangular channel (D and E) with a cross section of 33.3 mm (width) × 10.0 mm (height, h), which was the same as in the experiments of Cherry *et al*. [9] and in the simulations of Ohlsson *et al*. [11] and Malm *et al*. [15]. The length of the acrylic channel was 87 times the channel height (h) to allow for a fully developed flow. The channel was connected to the diffuser inlet, which was of the same cross-sectional dimensions. The entire diffuser section (E and F) was constructed using the same dimensions as specified in Cherry *et al*. [9]. The diffuser section was assembled using acrylic plates which were CNC machined for high-dimensional accuracy. Sufficient care was taken to avoid any surface irregularities. The outlet of the diffuser section was then connected to an acrylic duct (F and G) with a square cross section of 40 mm × 40 mm. The square duct connected to an outlet section (G and H), which consisted of a gradual diverging duct,

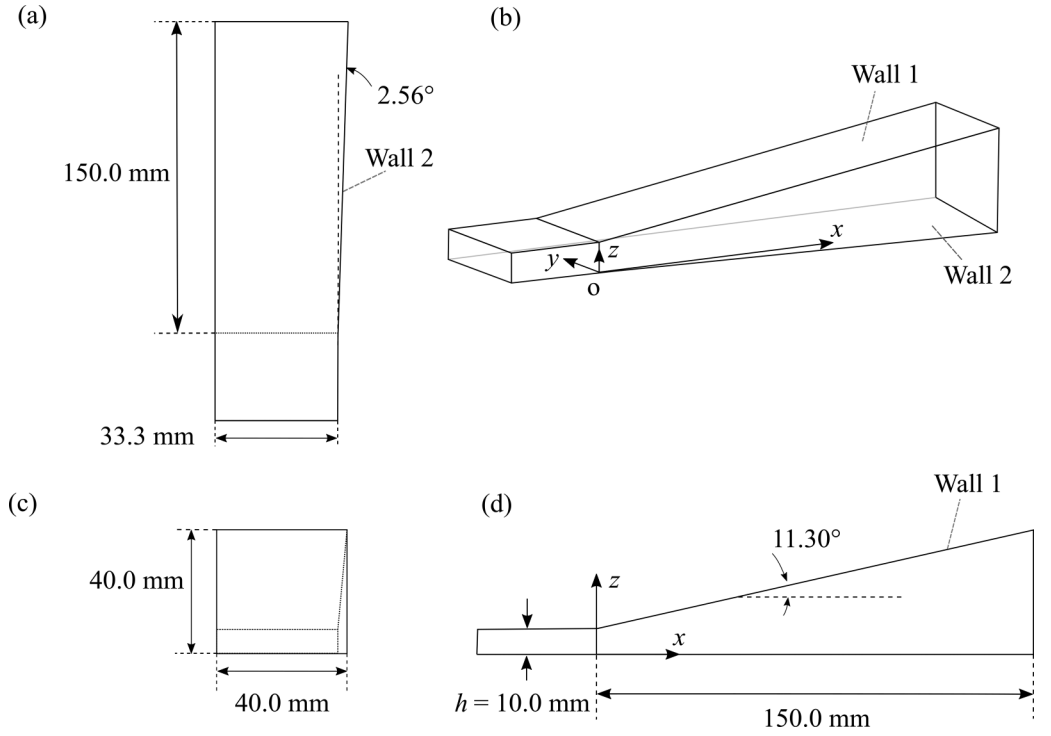

FIG. 1. Schematic showing the diffuser geometry studied in the present paper. The geometry is identical to the one devised by Cherry *et al*. [9]. The different views shown here are (a) top, (b) isometric, (c) front, and (d) side view.

a settling chamber, and another converging duct to connect to the reservoir using PVC pipes. The coordinate system adopted in the present study is also repeated in Fig. 2, with the y axis being normal to the plane of the paper and the origin (o) being at the diffuser throat. Prior to each measurement, the flow was circulated at the desired Re for a sufficiently long period of time (approximately 15 minutes) to de-air the loop and to ensure that there were no startup-related unsteadiness in the flow. Measurements were made for five different Re, the details of which are tabulated in Table I and are further detailed in Sec. III.

B. Planar PIV

Two-component PIV measurements of the flow field were carried out at upstream of the diffuser inlet (FOV 1) and in the diffuser section (FOV 2), as shown in Fig. 3(a).

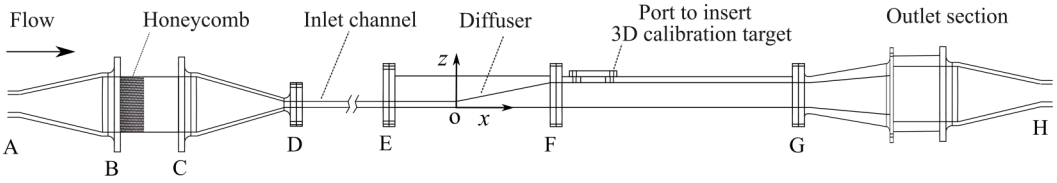

FIG. 2. Schematic showing an outline of the flow conditioning and diffuser sections used in the present paper. The flow loop also consists of a reservoir and a pump that are omitted from the schematic for clarity.

TABLE I. Inlet flow characteristics for the different Re cases studied.

Re	U_b (m s^{-1})	u_τ(m s^{-1})	λ (μm)
9200	0.92	0.055	18.0
14 400	1.44	0.078	12.8
19 200	1.92	0.099	10.1
24 000	2.40	0.121	8.2
29 400	2.94	0.143	6.9

The measurements at the inlet were made to verify if the boundary condition was a fully developed turbulent channel flow. To maintain consistency with the velocity profiles of previous numerical simulations [11], measurements were made for all Re at approximately $6h$ upstream of the diffuser throat ($x/h = -6$). The field of view of the measurements at the inlet (FOV 1) was approximately $0.3h$ and h in the x and z directions, respectively, at $y/h = 1.65$, which is the midplane of the channel.

The measurements of the diffuser section were made for comparison with 3D-PTV measurements at Re 9200. For this, the length of FOV 2 was chosen to be approximately $7h$ in the streamwise direction at $y/h = 1.65$ and covered the entire diffuser in the z direction, as marked using dotted lines in Fig. 3(a). The location of FOV 2 was between $x/h = [3.5\ 10.5]$.

For all planar measurements, a dual cavity Nd:YLF high-speed laser (Photonics Industries DM20-527-DH) was used in combination with mirrors and a cylindrical lens to generate a laser sheet, which illuminated the measurement plane. The laser had a wavelength of 527 nm and pulse energy of 20 mJ per cavity. The thickness of the sheet was approximately 1 mm. A high-speed CMOS camera (Phantom V611) with a sensor size of 25.6 mm $\times$ 16.0 mm and pixel size of 20 μm was used. The camera had a maximum resolution of 1280 $\times$ 800 pixels and was equipped with a 105 mm lens to image the flow field. The laser was synchronized with the camera using a programmable timing unit (PTU X, LaVision, GmbH). The flow was seeded using 2-μm silver-coated glass spheres with a relative density of 2.6 gm/cc (Potters Industries).

For the inlet velocity measurements at FOV 1, double-frame images were recorded at 200 Hz with different time delays between laser pulses based on Re. The latter was to obtain a maximum

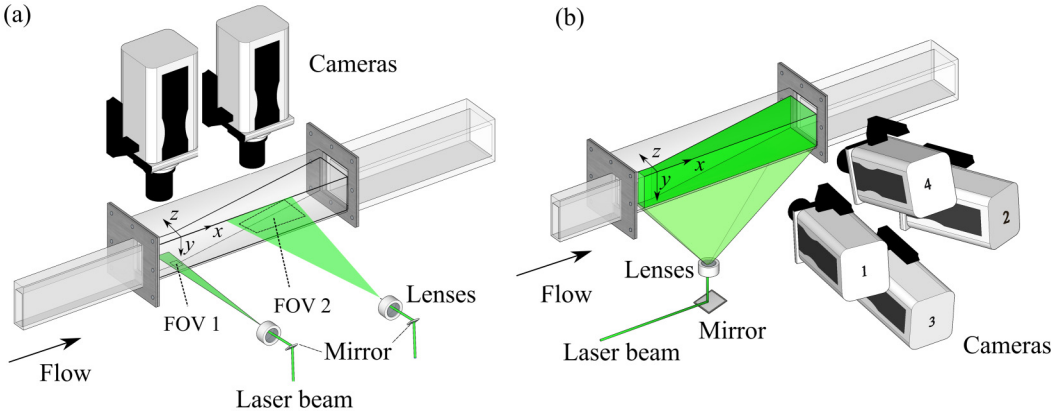

FIG. 3. A schematic of the experimental setup used for (a) planar PIV and (b) 3D-PTV measurements. The coordinate axes used are as shown in the figure. In (a), a laser sheet is directed along the xz plane to illuminate the midplane ($y/h = 1.65$) for both FOV 1 and FOV 2. In (b), the FOV shown is illuminated using volumetric expansion of the laser beam.

particle displacement of approximately ten pixels for all Re. The images were calibrated to scale using the diffuser inlet height (h). The digital resolution of the captured images was 9.38 μm/pixel at an imaging magnification of 2.12. To obtain statistical convergence, a total of 6000 double-frame images were recorded over a duration of 30 seconds for each Re. The images were enhanced by subtracting the minimum of the entire ensemble to remove background intensity. To further improve the signal-to-noise ratio, the resulting images were multiplied with a constant and were then normalized with the average intensity of the entire data set. The images were then cross correlated using the ensemble-of-correlation method [27] in Davis 8.4 (LaVision GmbH). This method allows for a significant improvement in the spatial resolution of the mean velocity field by averaging the instantaneous correlation functions, instead of averaging the instantaneous velocity fields. Such a method has even been implemented in the past to achieve resolutions in the range of a single pixel [28]. In the present case, the final window size for mean flow field was 6 $\times$ 6 pixels with 75% overlap of the windows. This allowed us to resolve the velocity field as close as three pixels from the wall, which corresponds to the first data point at approximately $z^+ = 1.5$ for Re 9200. The instantaneous flow fields for Reynolds stress estimation were calculated using double-frame cross correlation with a final window size of 32 $\times$ 32 pixels and 75% window overlap. This resulted in data points as close as 16 pixels or $z^+ = 8$ for Re 9200.

For FOV 2, a total of 140 000 single frame images were recorded at 1500 Hz, with the digital resolution and magnification of the images being 57.1 μm/pixel and 0.35, respectively. The image enhancement steps applied to these images were the same as described above for FOV 1. The improved images were then cross correlated to get instantaneous velocity fields with a final window size of 24 $\times$ 24 pixels and 75% overlap of the windows.

C. 3D-PTV using shake-the-box

The turbulent flow field in the diffuser section was characterized using time-resolved, 3D-PTV. Figure 3(b) shows a schematic of the setup used. The same laser and cameras used for planar PIV were used here, although for 3D measurements, four high-speed cameras (Phantom V611) were used. For volumetric illumination, the laser beam was expanded into a volume using a combination of spherical and cylindrical lenses, resulting in an illuminated domain that encompasses the entire diffuser section as shown schematically by the green colored region in Fig. 3(b). The four cameras were arranged in a configuration such that cameras 1 and 2, as shown in Fig. 3(b), were approximately on the xz plane while camera 3 was below and camera 4 was above the xz plane. Four 50-mm lenses were connected to the cameras using Scheimpflug adapters. All four cameras had an aperture setting of $f/16$ to ensure that the domain fell within the depth-of-field of the camera. Target calibration for mapping the measured volume was carried out using a dual-plane target (89 mm $\times$ 21 mm $\times$ 4 mm) with the two planes separated by 1 mm. The target was placed inside the diffuser section through a port shown in Fig. 2. The diffuser was filled with water and the target was held parallel to the xz plane using a custom-made mount. The target was traversed along the z axis to obtain an additional view 1 mm apart. An initial mapping function was obtained using a third-order polynomial fit. The digital resolution of the captured images was 84.7 μm/pixel with a magnification of 0.24.

The flow was seeded using polyethylene microspheres (CoSpheric, USA) with an average diameter of 82.5 μm and an absolute density of 1250 kg/m^3. This relatively larger particle size, when compared to those for planar measurements, was necessitated by the volumetric expansion of the laser beam over the entire FOV, which results in lower light intensity. Since the main objective of this paper is to investigate large-scale flow structures in the diffuser region, a Stokes number based on the fluid bulk velocity and inlet channel height is relevant. The particle Stokes number (Stk) is evaluated using τ_p/τ_f, where τ_p and τ_f are the particle response time and flow timescale, respectively. This estimation is approximately 0.02 for the highest Re case studied (Re = 29 400), which implies that the particles faithfully follow the large-scale flow within the diffuser region (Stk $<<$ 1) for the range of Re considered. The relaxation time, $\tau_p = (\rho_p - \rho_f)d_p^2/18\mu$, for these

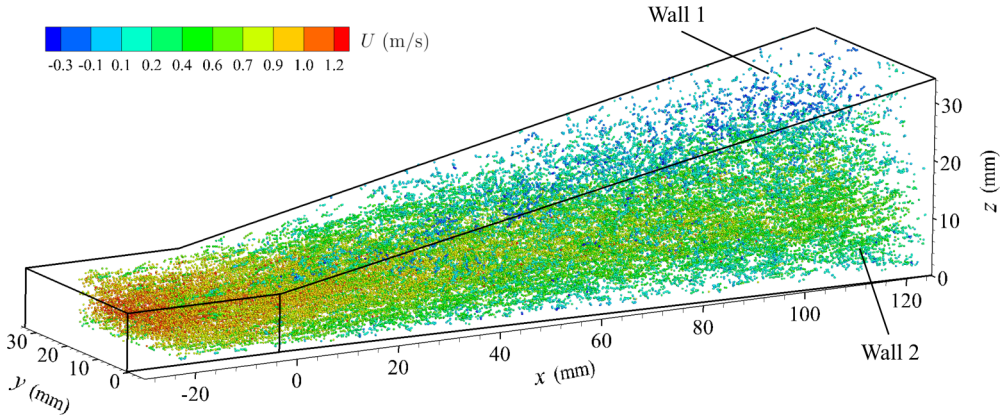

FIG. 4. Instantaneous particle tracks for the Re = 9200 case. The particle tracks shown here are from five successive time instants, with the time step being 0.66 ms at 1.5 kHz. The particles are color coded using their streamwise velocity magnitudes.

particles is estimated to be 94 μs, where ρ_p and ρ_f are the particle and fluid density respectively. This results in a terminal velocity of 0.9 mm/s and a particle Reynolds number of 0.075. The Kolmogorov timescale of the flow (τ_κ) is estimated using the turbulence measured at the channel centerline (presented in Sec. III). The method adopted is similar to Kussin and Sommerfeld [29] and uses approximate expressions for turbulent kinetic energy, $k = 0.5\ (\langle u^2\rangle + 2\langle w^2\rangle)$, and dissipation rate, $\epsilon = C_\mu^{0.75} k^{1.5}/l_m$, where C_μ and l_m are taken to be 0.09 and $0.07h$, respectively. The Kolmogorov timescale, $\tau_\kappa = \sqrt{(\nu/\epsilon)}$, for Re = 29 400 is then estimated to be approximately 0.82 ms.

Single-frame images were acquired at a high frequency (ranging between 1.5 kHz to 3.5 kHz), depending on the Re. The total duration of flow captured using multiple sets of data ranged between approximately 6.5 seconds (for Re = 29 400) to 26.5 seconds (for Re = 9,200). The recorded images were processed using commercial software (DaVis 10, LaVision GmbH). As a first step, the minimum of the recorded ensemble of images was subtracted from each image to remove the background intensity. Further, the resulting images were normalized with the average of the ensemble. The images were also improved by subtracting a sliding minimum over five pixels and normalizing with a local average over 500 pixels. After these image enhancement steps, a volume self calibration process was applied to remove the initial calibration disparities [30] and to calculate the optical transfer function [31]. Finally, particle tracks were calculated using the STB algorithm to obtain Lagrangian particle tracks in the diffuser section within a total measurement volume of approximately 165 mm × 35 mm × 35 mm. The maximum particle shift in the algorithm was set to 8 voxels with an allowed triangulation error of 1 voxel. If the particles were found to be closer than 1 voxel, they were removed to inhibit calculation of erroneous tracks. To identify the diffuser wall locations, we used MART of the minimum intensity of the ensemble of images [32]. The minimum intensity image included small glare points from the internal surface of the diffuser, which after 3D reconstruction, indicate the boundaries of the diffuser. The wall 1 and wall 2 coordinates were then estimated using image slices parallel to the yz and xy planes, respectively.

The average number of particle tracks captured for each time step was approximately 8000 from images with a particle density of approximately 0.04 particles per pixel. The particle velocity was computed by fitting a second-order polynomial to the particle locations with a filter length of five time steps [24]. A volumetric visualization of the particle tracks obtained using the measurements is shown in Fig. 4. The particle tracks presented in the figure are a superposition of five successive time instants at 1500 Hz. The color code is based on the particle's streamwise velocity. An animation of the Lagrangian particle tracks in time is also presented as Supplemental Material [33].

The accuracy of velocity measurements from 3D-PTV depends primarily on the error in detecting the particle peak locations. This error is estimated to be approximately of the order of 0.1 pixel for the in-plane components and 0.2 pixels for the out of plane component, based on the analysis by Abu Rowin and Ghaemi [34] on a similar 3D-PTV system. This corresponds to uncertainties in the U and V components to be approximately 1.9% and in the W component to be approximately 3.8% of the bulk velocity for Re 9200.

The particle tracks were then projected on a 3D grid, resulting in a 3D Eulerian velocity field. To achieve this, particles were binned over a 3D Cartesian grid with anisotropic bins of 5 mm $\times$ 1.5 mm $\times$ 1.5 mm in the x, y, and z directions, respectively, and an overlap of 50% in each direction. To obtain a more accurate evaluation of the Reynolds stress distribution, a second-order polynomial fit was applied to the velocity distribution within each bin to evaluate the velocity fluctuations [35]. Instantaneous as well as mean velocity fields were computed for each Re. The data in the inlet section preceding the diffuser was also binned separately with a higher resolution using anisotropic bins of dimensions 5 mm $\times$ 0.5 mm $\times$ 0.5 mm in the x, y, and z directions respectively. A brief discussion on the statistical convergence of the data is presented in Appendix.

For the investigation of the near-wall flow topology, we evaluated the velocity field close to and parallel to the diverging walls. Near-wall streamlines, if sufficiently close to the wall, are topologically consistent with skin-friction lines [22]. In the present paper, we aim to identify large-scale patterns in the skin-friction lines that could be directly connected to the 3D flow topology in the diffuser. For this purpose, the diffuser wall coordinates are discretized to generate bins which are in the form of cuboids with dimensions 2.5 mm $\times$ 2.5 mm $\times$ 1 mm and 50% overlap, with the smallest dimension being in the wall-normal direction. This is done for each wall separately to generate bins which are parallel to the corresponding wall. The binning of particles close to the wall then results in velocity fields on planes 0.5 mm away from and parallel to each wall. In the present paper, we will refer to the near-wall streamlines as skin-friction lines.

The notations used in the subsequent sections are as follows. Variables enclosed within $\langle\,\rangle$ denote a time average. The uppercase letters U, V, and W denote the instantaneous velocity components in the x, y, and z directions, respectively. The corresponding lowercase letters (u, v and w) denote the velocity fluctuation components, such that the instantaneous vector field $\boldsymbol{U}(\boldsymbol{x}, t) = \langle \boldsymbol{U}(\boldsymbol{x}, t)\rangle + \boldsymbol{u}(\boldsymbol{x}, t)$. The superscript ($^+$) on a variable is used to denote normalization using inner scaling.

D. Modal decomposition

The measured 3D flow field is analyzed using a modal decomposition to identify large-scale structures in the flow. To this end, we employ a spectral proper orthogonal decomposition (SPOD) for the Re 9200 case to investigate the temporal characteristics of dominant modes. This section provides a brief description of this method.

The SPOD of the turbulent flow field is useful toward identifying spatiotemporal modes unique to a single frequency [36]. The analysis used here follows the method detailed in Towne *et al.* [36] and has its basis on previous works of Lumley [37] and Picard and Delville [38]. SPOD involves seeking a set of orthogonal functions $\boldsymbol{\varphi}(\boldsymbol{x}, t)$ under the assumption that the turbulent flow is statistically stationary. This entails solving an eigenvalue problem given as

$$\int_{-\infty}^{\infty}\int_{V} \boldsymbol{C}(\boldsymbol{x}, \boldsymbol{x}', t, t')\boldsymbol{\varphi}(\boldsymbol{x}', t')d\boldsymbol{x}'dt' = \lambda\boldsymbol{\varphi}(\boldsymbol{x}, t), \tag{1}$$

where $\boldsymbol{C}(\boldsymbol{x}, \boldsymbol{x}', t, t')$ is a two-point space-time correlation tensor given by $\boldsymbol{u}(\boldsymbol{x}, t) \otimes \boldsymbol{u}(\boldsymbol{x}', t')$, defined at two locations $(\boldsymbol{x}, \boldsymbol{x}')$ and at two times (t, t'). Under the stationarity assumption, this is equal to $\boldsymbol{C}(\boldsymbol{x}, \boldsymbol{x}', \tau)$ with $\tau = t - t'$. If we now take a Fourier transform of this tensor, we get a cross-spectral density (CSD) tensor written as

$$\boldsymbol{S}(\boldsymbol{x}, \boldsymbol{x}', f) = \int_{-\infty}^{\infty} \boldsymbol{C}(\boldsymbol{x}, \boldsymbol{x}', \tau)e^{-i2\pi f t}d\tau, \tag{2}$$

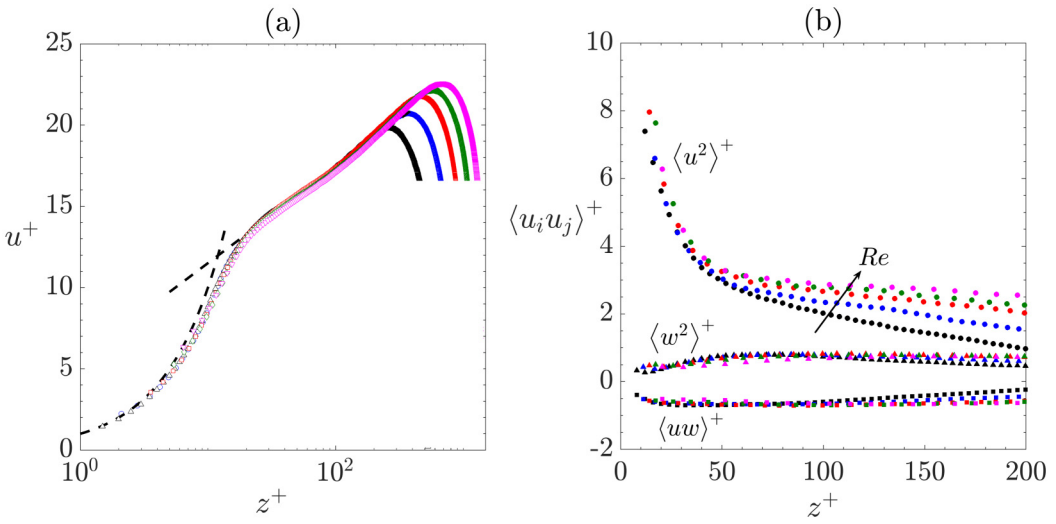

FIG. 5. (a) Near-wall log law for different Re cases, with Re = 9200 (Δ), 14 400 (○), 19 200 (□), 24 000 (◇), 29 400 (∇). (b) Reynolds stress components for different Re. The normal stresses $\langle u^2 \rangle$ and $\langle w^2 \rangle$ are denoted by circles and triangles, respectively, whereas the shear stress $\langle uw \rangle$ is denoted by squares. The different Re values shown are 9200 (*black*), 14 400 (*blue*), 19 200 (*red*), 24 000 (*green*), and 29 400 (*magenta*).

where f is the frequency. The CSD tensor can now be used to define an eigenvalue problem in the spectral domain,

$$\int_V \boldsymbol{S}(\boldsymbol{x}, \boldsymbol{x}', f')\boldsymbol{\psi}(\boldsymbol{x}', f')d\boldsymbol{x}' = \lambda f' \boldsymbol{\psi}(\boldsymbol{x}', f'), \tag{3}$$

where the eigenvectors $\boldsymbol{\psi}(\boldsymbol{x}, f)$ of the CSD tensor are the SPOD modes at a specific frequency f'.

For the SPOD analysis in the present paper, we use a total of $N_t = 2180$ instantaneous snapshots, with a sampling frequency of $f_s = 300$ Hz. This entire sequence was segmented into six blocks ($N_{\text{blk}} = 6$), each with $N_{\text{FFT}} = 1024$ snapshots and a block overlap of $N_{\text{ovlp}} = 800$ snapshots. This results in a frequency resolution of $f_s/N_{\text{FFT}} = 0.29$ Hz, or St = 0.003. For SPOD, N_{FFT} needs to be sufficiently long to achieve reasonable frequency resolution, and N_{ovlp} decides the number of blocks, N_{blk} [39].

III. INLET FLOW CHARACTERISTICS

The flow in the straight channel was measured using planar PIV along the xz plane at a distance approximately $6h$ upstream of the diffuser as highlighted in Fig. 3(a). The normalized streamwise velocity ($u^+ = \langle U \rangle / u_\tau$) in the channel as a function of the wall coordinates ($z^+ = z/\lambda$) is shown in Fig. 5(a). Here, the inner scaling is estimated by using the Clauser method [40], which fits the measured velocity profile in the logarithmic region as $u^+ = 1/\kappa \, lnz^+ + C$. The log-law constants are assumed to be $\kappa = 0.39$ and $C = 5.6$. We then verify that the data points also follow $z^+ = u^+$ in the linear viscous sublayer for all Re. This shows that for all Re the inlet flow is a fully developed turbulent channel flow. This criterion is important for consistency with the boundary conditions applied in the numerical simulations [11]. The friction velocity (u_τ) and wall unit (λ) for different Re are then estimated using this fit and are presented in Table I. The inlet bulk velocity (U_b) for each Re is also estimated from 3D-PTV measurements and is presented in Table I. The maximum uncertainty in particle displacement in the PIV measurements is approximately 0.1 pixel [41], which corresponds to a maximum uncertainty of $0.17u^+$. These limits are of the order of the symbol size used in Fig. 5(a) and are therefore omitted.

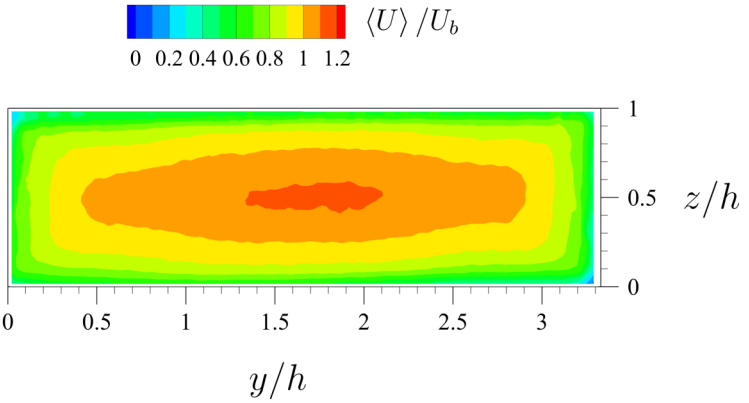

FIG. 6. Streamwise velocity contours from 3D-PTV measurements. The cross section shown is at approximately $4h$ before the diffuser throat.

Figure 5(b) shows the Reynolds stresses as a function of the wall-normal coordinate for different Re. The observed trend for the three different stress components shown here matches well with that observed for turbulent channel flows [42,43], wherein the $\langle u^2 \rangle^+$ values in the outer layer increases with Re. The typical range of peak $\langle u^2 \rangle^+$ values (between 6–8) observed here are similar to the range reported in Lee and Moser [43], with the peak values occurring at a z^+ of approximately 15. The trends of the other two components presented here, with peaks of $\langle w^2 \rangle^+$ (approximately 0.75) and $\langle uw \rangle^+$ (approximately -0.7) being similar to what has been previously reported for turbulent channel flows [42].

The streamwise velocity contours from 3D-PTV measurements at a cross-flow plane of $4h$ prior to the diffuser throat are shown in Fig. 6. It can be noted from the figure that the streamwise velocity appears symmetric about $y/h = 1.65$ and $z/h = 0.5$. We also note that these contours appear qualitatively similar to that shown by Cherry *et al.* [9]. Based on the experiments of Cherry *et al.* [9] and in the simulations of Ohlsson *et al.* [11], the inlet flow also consists of weak secondary flows. However, the magnitude of these secondary flow velocities was small and was of the order of approximately 3% of the average streamwise velocity [9]. These magnitudes translate to pixel displacements of the order of 0.1 pixel between two consecutive images in the present experiments. Such small displacements are typically in the lower limit of PTV measurement uncertainty and therefore cannot be captured here.

IV. FLOW IN THE DIFFUSER SECTION

In this section, we present the flow characteristics in the diffuser section. The analysis presented here is largely for the Re = 9200 case, however, we also present quantitative analysis across all Re cases studied. Comparisons of the Re = 9200 case are made with previous experimental [9] and DNS [11,15] results at Re = 10 000.

A. Mean flow

To give a qualitative description of the mean flow in the diffuser section, we present iso-contours of streamwise velocity for the Re = 9200 case in Fig. 7. The two isocontours shown in the figure are at $\langle U \rangle / U_b = 0.8$ (blue) and $\langle U \rangle / U_b = -0.03$ (red). Also presented in the figure is a slice of a yz plane at $x/h = 12$, wherein we plot the contours of streamwise velocity magnitude along with the cross-flow streamlines on the yz plane. The blue isocontour shows a region of high streamwise velocity, which is uniformly distributed in the inlet of the diffuser. As we move downstream, we see that this isosurface narrows into a thin region and disappears after approximately $x/h = 8$. The red

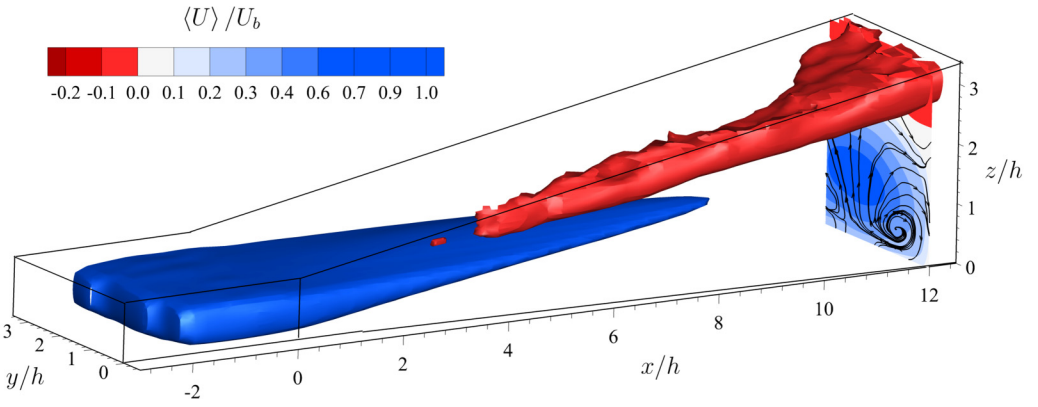

FIG. 7. Isosurfaces showing streamwise velocity for the Re = 9200 case. The isosurfaces shown here are at $\langle U \rangle / U_b = 0.8$ (blue) and -0.03 (red).

isocontour of streamwise velocity highlights the reverse flow region in the diffuser section which is close to the common corner of the two diverging walls, wall 1 and wall 2. This is henceforth referred to as the sharp corner, following Cherry *et al.* [9]. This asymmetry has been reported both in the experiments of Cherry *et al.* [9] and in the simulations of Ohlsson *et al.* [11]. The separated region spreads in the y direction as we move further downstream and remains aligned with the top diverging wall [9,11]. The in-plane streamlines of the $x/h = 12$ cross section shows the presence of a secondary flow in the diffuser region. A more detailed observation on this flow aspect is made later in this section. We briefly note that the top surface of red isocontours in Fig. 7 suggests lack of statistical convergence. This is primarily because the bins close to the diverging walls are not parallel to the wall. This results in portions of the bins being outside of the measurement domain, which results in fewer particles in the bins. In contrast, the statistics for bins that are completely inside the measurement volume are converged (see Appendix). This issue was addressed for the near-wall analysis in later sections by generating bins parallel to the walls, as explained previously in Sec. II C.

Figure 8 shows mean streamwise velocity contours at different sections across the diffuser. Specifically, Fig. 8(a) shows a section along the xz plane at $y/h = 1.65$ (midspan of the diffuser inlet) whereas (b)–(d) show the cross-flow slices at $x/h = 2$, 8, and 12, respectively. In Fig. 8(a), the mean streamwise velocity profiles are also plotted using dotted lines at a few selected streamwise locations. The locations $x/h = 8$ and 12 are chosen to also plot the velocity profiles from the simulations of Ohlsson *et al.* [11] shown as red dots. A thick black line is drawn at the loci of streamwise velocity to identify the backflow region. Broadly, the velocity profiles and the zero velocity contour enclosing the separation region agree reasonably well with the experiments of Cherry *et al.* [9]. The zero velocity contour line appears at approximately $x/h = 8$, and the velocity profiles and contours clearly highlight the reverse flow region thereafter. The comparison with the DNS profiles also shows reasonable agreement with the largest differences in the streamwise velocity being approximately 8% of the bulk velocity. A comparison of the velocity contours and profiles made with planar PIV measurements, which are shown in the inset of Fig. 8(a), also show a good agreement.

As noted previously from the 3D isosurfaces of mean velocity, the separation region is asymmetric and the flow separates before $x/h = 8$ close to the sharp corner. This can be better visualized from the cross-flow slices presented in Figs. 8(b)–8(d). At $x/h = 2$ in Fig. 8(a), we note that a region of reverse flow starts appearing in the corner which connects the two diverging walls. As we move further downstream in Figs. 8(c) and 8(d), we note that the backflow region grows in the y direction and covers the entire top wall.

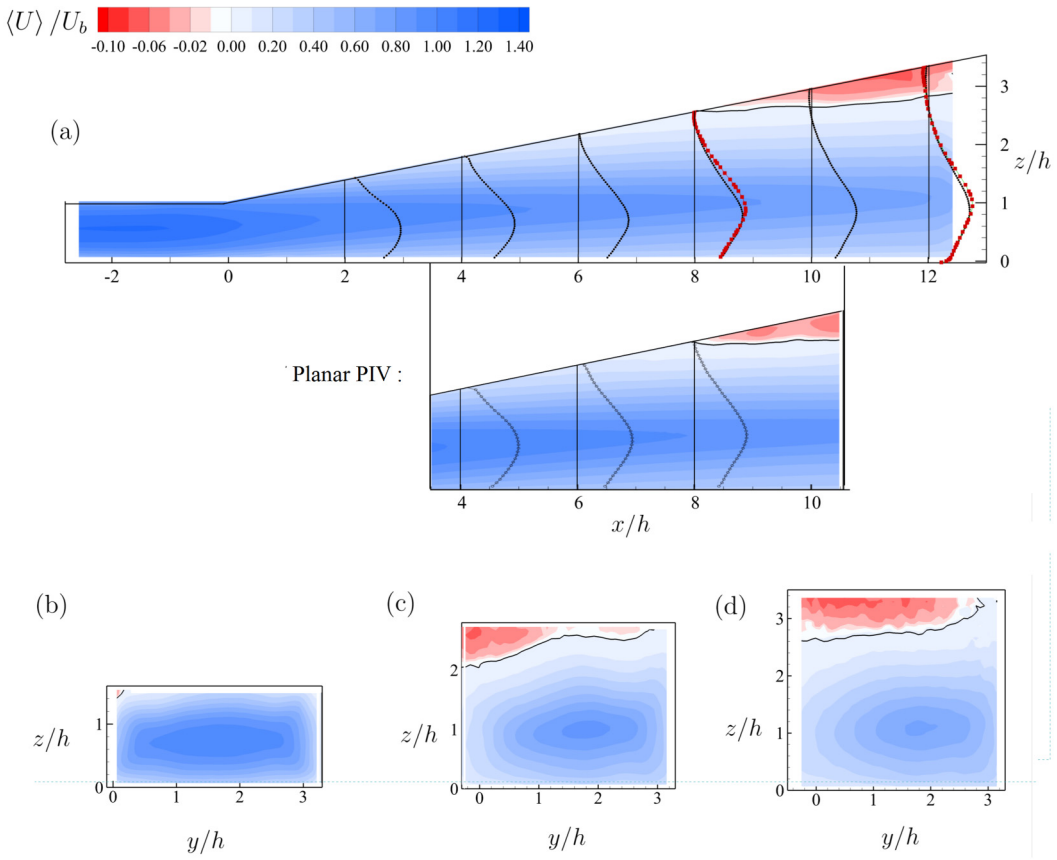

FIG. 8. Mean flow contours of streamwise velocity for the Re = 9200 case. (a) shows an xz section at the y center plane of the diffuser section. The zero velocity contour is shown as a thick solid line. The mean streamwise velocity profiles at six different streamwise locations are superimposed on the velocity contour plot, along with the velocity profiles (red dots) at $x/h = 8$ and 12 from the DNS of Ohlsson *et al.* [11]. The inset of (a) shows the same plot from planar PIV measurements. The cross-flow (yz) slices at three different streamwise locations are shown at $x/h =$ (b) 2, (c) 8, and (d) 12.

Figure 9 shows the streamwise location of the separation point x_s as a function of Re. The separation location shown here is detected at the $y/h = 1.65$ plane of the diffuser. With increasing Re, the location at which backflow starts in this cross section appears to move upstream, with the maximum variation in the distance between the lowest and highest Re being approximately 10% of the diffuser length. It should also be noted that this variation is at a single cross section whereas the separation surface in this configuration would be entirely 3D in nature.

B. Intermittency

To investigate the unsteadiness of the separation front, we plot contours of an intermittency factor (γ) in Fig. 10 at the same cross sections shown previously in Fig. 8. This intermittency factor is defined as the fraction of time the flow moves in a downstream direction at a given location [44]. Based on this definition, a value of $\gamma = 0.99$ signifies *incipient detachment* (ID) wherein backward flow occurs 1% of the time. *Intermittent transitory detachment* (ITD) is defined at $\gamma = 0.8$ and *transitory detachment* (TD) at $\gamma = 0.5$. The detachment (D), where the time-averaged wall shear stress is zero, and TD occur approximately at the same location [1]. In Fig. 10, the location of ID,

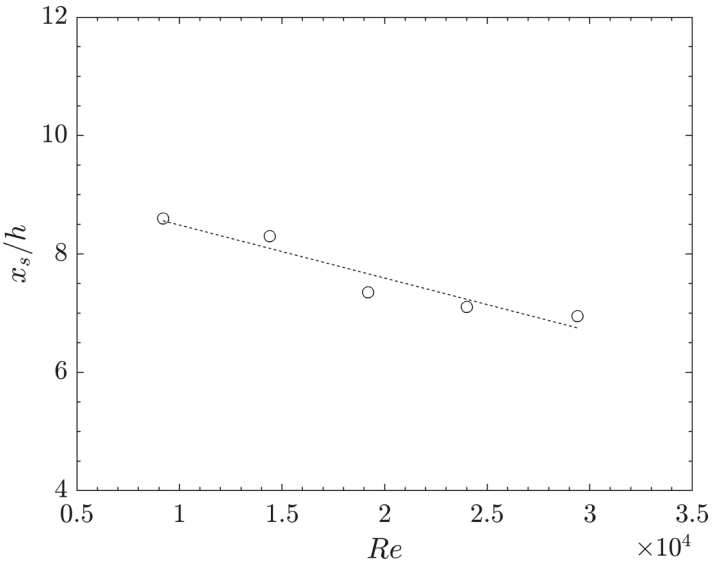

FIG. 9. The streamwise location of the separation point (x_s) in the $y/h = 1.65$ plane as a function of Re. The dotted line is a linear fit to the data.

ITD and TD are drawn using black lines at each cross section with the corresponding γ value labels. We note that the probability of reverse flow grows higher in the downstream direction and closer to wall 1 in Fig. 10(a). The ID line in this cross section originates at around the diffuser throat and then follows close and parallel to wall 1 up until approximately $x/h = 2.5$. After $x/h = 4$, the ID line remains nearly parallel to the bottom wall at a height $z \approx 1.6h$. The ITD line appears near $x/h = 3.5$ at wall 1, and remains close to $z \approx 2.2h$ as we move further downstream. The inset in Fig. 10(a) shows the measurements from planar PIV. A comparison with the 3D-PTV measurements show that the TD line appear to originate at similar streamwise location of $x/h = 8$ in both cases. However, the origin of the ID and ITD is farther downstream near $x/h = 5$ and $x/h = 7$, respectively, in the planar measurements. It should be noted that the duration of measurement in 3D-PTV is approximately three times that of the planar measurements. This suggests that the ID and ITD are captured more accurately in 3D-PTV measurements because of sufficiently long acquisition time.

The cross-flow sections in Figs. 10(b)–10(d) further highlight the asymmetric nature of the flow, with the reverse flow being more probable to occur close to the sharp corner. The ITD appears in the sharp corner at $x/h = 2$, and the region with $\gamma \leqslant 0.8$ becomes more dominant as we go further downstream. The reverse flow with $\gamma \leqslant 0.5$ occurs frequently near the top wall at $x/h = 8$ and further downstream. At $x/h = 8$, there are two small regions of $\gamma \leqslant 0.5$, which appear to merge into a larger region by $x/h = 12$. These observations match with the cross-flow sections of γ shown in the numerical simulations of Malm *et al.* [15].

In Fig. 11, we show the contours of γ at different cross-flow sections for Re of 19 300 and 29 400. Figures 11(a)–11(c) are for Re = 19 300 at $x/h = 2$, 8, and 10, respectively, whereas (d) and (e) are for Re = 29 400 at the same cross-flow sections. We note that the contours of γ appear similar for the Re = 19 300 case when compared with the Re = 9200 case, with there being no significant variations in the mean velocity contours (not shown here for brevity). However, when we compare with the Re = 29 400 case, we find marginally less intermittency probability (i.e., more forward flow) in the separated region. To view this more quantitatively, we next plot in Fig. 12 the volume fraction with the 3D isocontour of ITD (i.e., with $\gamma < 0.8$) relative to the diffuser volume up until $x/h = 12$. We note that with increasing Re, the fraction of volume with $\gamma < 0.8$ reduces by approximately 9% between Re = 9200 and 29 400.

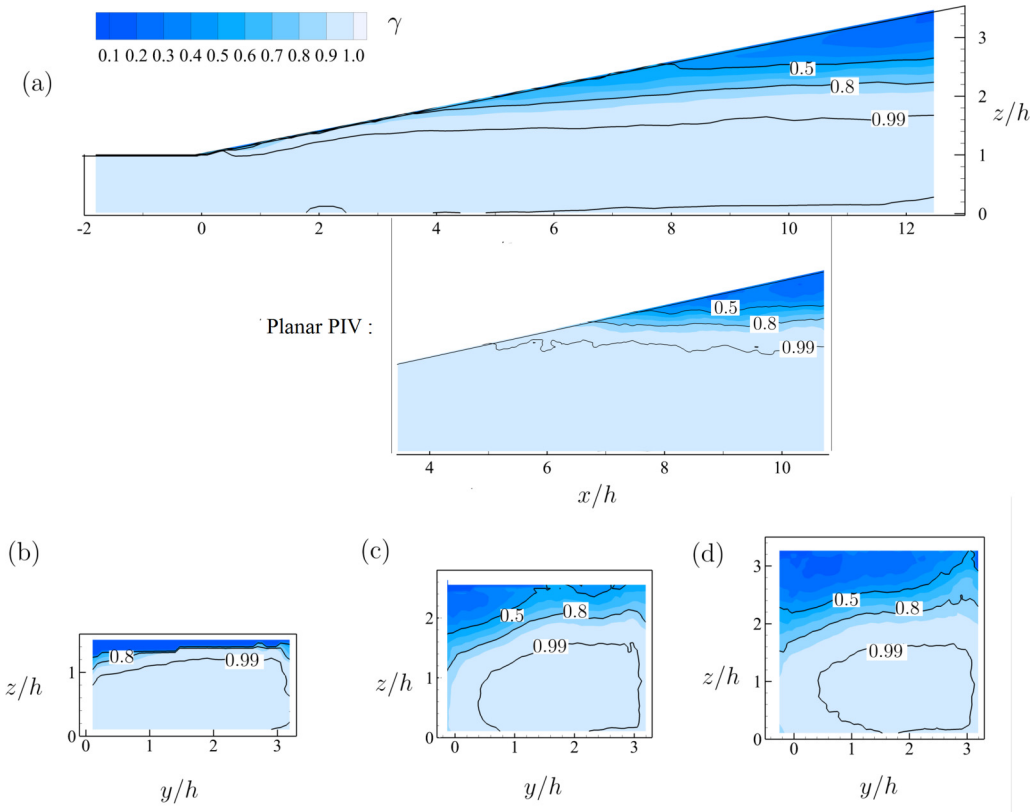

FIG. 10. Contours of the intermittency factor γ for the Re = 9 200 case. (a) shows an xz section at the y center plane of the diffuser section, and the inset shows the same measurements from planar PIV. The cross-flow sections at three different streamwise locations are shown at $x/h =$ (b) 2, (c) 8, and (d) 12.

C. Secondary flow

Figure 13(a) shows the isosurfaces of mean streamwise vorticity $\langle\omega_x\rangle$ to highlight the secondary flow features. The isosurfaces of streamwise vorticity $\langle\omega_x\rangle$ in (a) show the secondary flow structures that start to develop in the channel upstream of the diffuser. Cherry *et al.* [9] and Ohlsson *et al.* [11] also showed the existence of a secondary flow, which initiated in the corners of the straight channel preceding the diffuser. Such secondary flows are found in turbulent flows through straight ducts with noncircular cross sections and arise due to Reynolds stress gradients in the cross-stream plane [45]. These secondary flows have been shown to be weak in magnitude and grow weaker with increasing Re [46]. The DNS of Malm *et al.* [15] show the persistence of the secondary flows well into the diffuser section in the form of corner vortices in the upper part of the diffuser which is closer to wall 1. In the present experiments, the streamwise vorticity is expected to be present in all four corners of the straight duct preceding the diffuser. However, we find that in the diffuser section, only the vorticity from the bottom corners of the straight wall persists well into the diffuser. This is in contrast to what was observed in the simulations of Malm *et al.* [15], wherein the streamwise vorticity from only the top corners were observed well in the diffuser. To show the secondary flow pattern more clearly, we plot the in-plane streamlines along with mean streamwise vorticity contours at a cross-flow plane of $x/h = 12$ in Fig. 13(b). The streamlines clearly show the bottom two vortices that represent the secondary flows. We can also note that the top left corner shows concentrated vorticity along with curved streamlines, suggesting the presence of a weak secondary flow vortex.

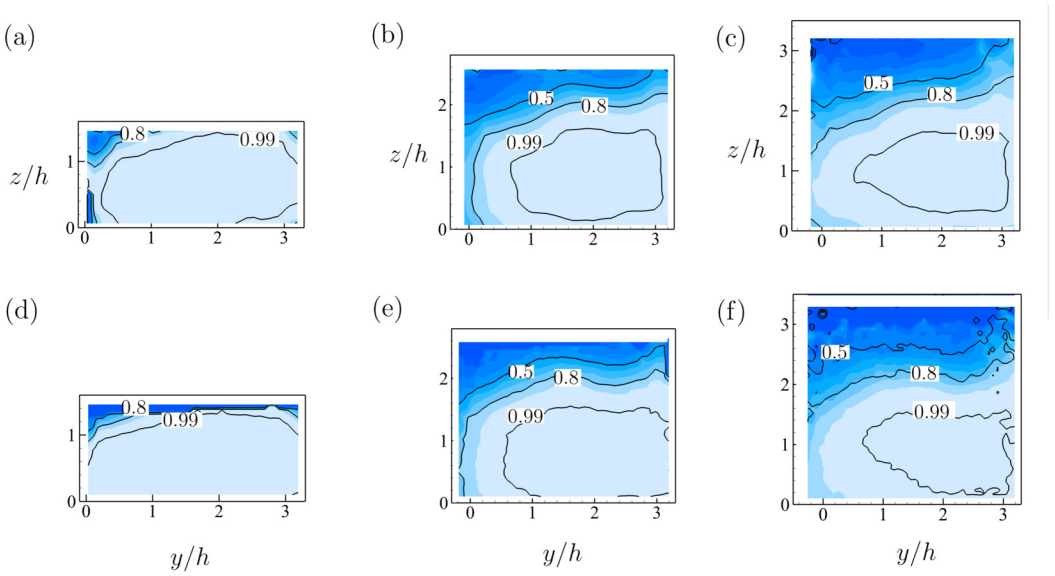

FIG. 11. Contours of intermittency factor (γ) for Re = 19 300 and 29 400 cases at different cross-flow sections. (a)–(c) are for Re = 19 300 at $x/h = 2$, 8, and 10, respectively. (d), (e) are for Re = 29 400 at $x/h = 2$, 8, and 10, respectively.

The vorticity in the top right corner, however, appears more diffused than the rest as no secondary vortex is detected. Malm *et al.* [15] also noted that the streamwise vorticity in the sharp corner diffuses rapidly due to higher turbulent diffusion.

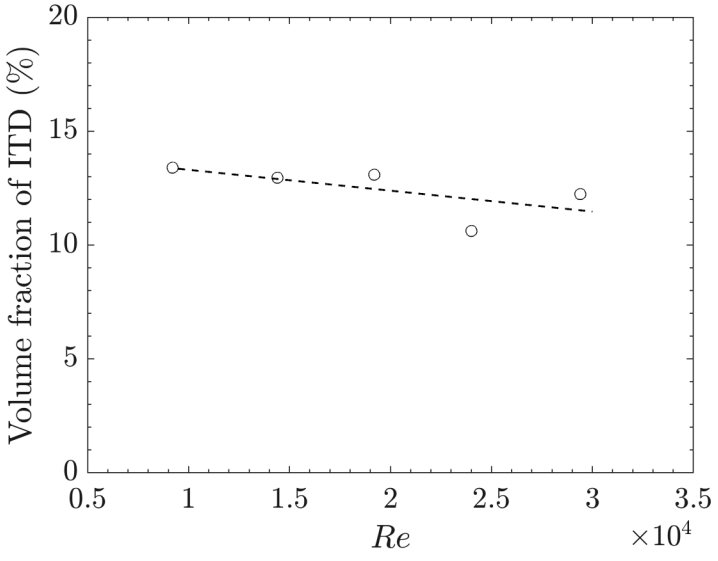

FIG. 12. The volume fraction of the diffuser section with $\gamma < 0.8$ as a function of Re. The dotted line is a linear fit to the data.

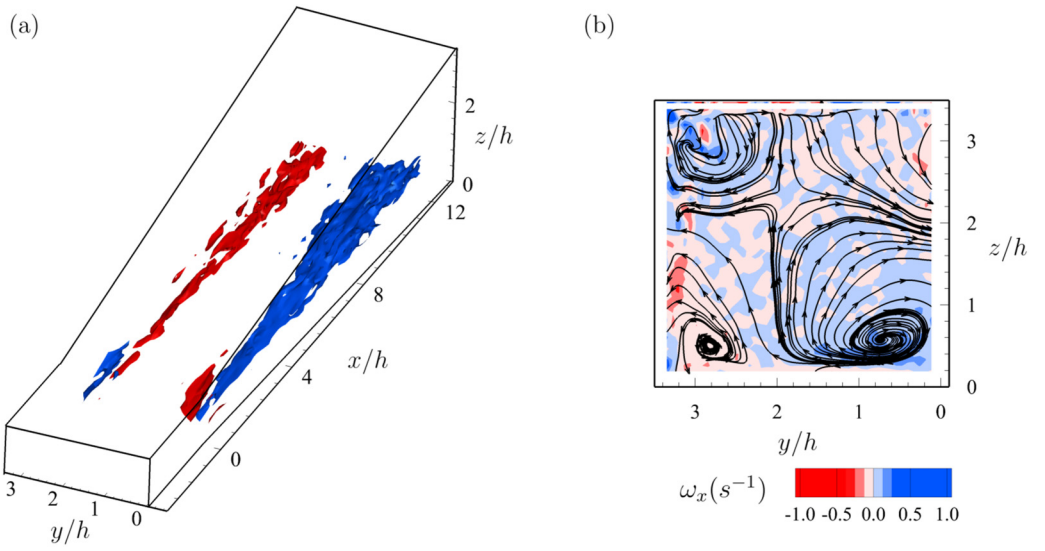

FIG. 13. (a) Isosurfaces showing streamwise vorticity $\langle\omega_x\rangle = \pm$ 0.1 s^{-1} contours. The colors red and blue signify negative and positive signs, respectively. (b) Cross-flow section at $x/h = 12$ showing in-plane streamlines superimposed on streamwise vorticity contours to highlight the secondary flow patterns.

Although not shown here, we find the existence of secondary flows across all Re cases, and the qualitative patterns remain similar to that shown in Fig. 13. The strength of the secondary flows as a function of Re can be estimated from the peak magnitude of the mean streamwise vorticity $\langle\omega_x\rangle$ for the two vortices seen along the bottom wall at $x/h = 12$. An average of the absolute magnitude of these two peak vorticities is plotted in Fig. 14 for all Re cases. Although the dimensional magnitudes of this averaged vorticity increased with increasing Re, upon normalizing, the average peak vorticity magnitude, $\langle\omega_x\rangle h/U_b$ appeared to reduce with increasing Re. This suggests that the secondary flow, even though persistent, weakens marginally relative to the bulk flow with increasing Re.

D. Reynolds Stresses

In this section, we present the distributions of Reynolds stresses in the diffuser section. In previous numerical simulations, it has been shown that modeling the Reynolds stress distributions is important for predicting the flow separation with accuracy [13]. For example, an assumption based on an isotropic flow condition would result in no secondary flows and therefore would not accurately model the separation behavior in the diffuser [13,15].

We start with presenting the normalized $\langle u^2\rangle$ contours in Fig. 15. The different sections shown in the figure are the same as for Fig. 8. In Fig. 15(a), we present a comparison between the 3D-PTV and the planar PIV measurement of $\langle u^2\rangle$. The planar measurements are shown as an inset below the contours from 3D-PTV, and range from $x/h = 3$ to $x/h = 10.5$, approximately. The comparison shows that qualitatively the trends appear similar, however, the $\langle u^2\rangle$ magnitudes in 3D-PTV measurements are higher than their planar counterpart. In the subsequent analysis, it should be noted that the Reynolds stress descriptions are suitable for qualitative analysis since their magnitudes could be different than the true values.

The xz plane shown in Fig. 15(a) shows that high $\langle u^2\rangle$ values are in the region which separates the reverse and forward flow. At the cross-flow section near the inlet [$x/h = 2$ in Fig. 15(b)], the region of high streamwise Reynolds stress remains close to the walls, with a slight asymmetry toward the sharp corner (top left) where flow separates. With increasing x, the region of high fluctuations shift toward the center. Specifically, the peak $\langle u^2\rangle$ values shifts from $y/h \approx 0.5$ to

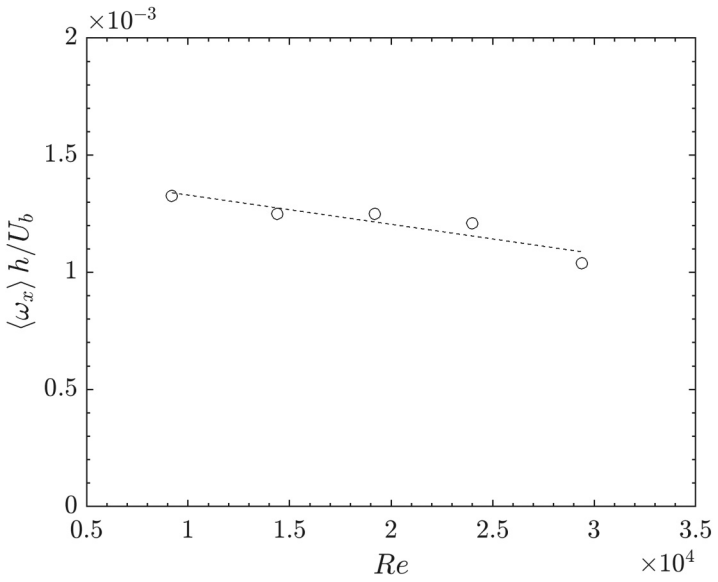

FIG. 14. The variation of the averaged peak streamwise vorticity of the secondary flow as a function of Re. The vorticity $\langle\omega_x\rangle$ is normalized by the bulk flow velocity (U_b) for each Re and the diffuser inlet width (h). The dotted line is a linear fit to the data.

$y/h \approx 2$ between Figs. 15(c) and 15(d). This region corresponds to the shear layer outside of the separation region. The separation region itself shows relatively lower streamwise fluctuations. The qualitative observations of the Reynolds stresses remain similar across all Re studied. To look at any quantitative variations, we plot the peak magnitude of normalized root-mean-square fluctuations of streamwise velocity, u_{rms}/U_b, as a function of Re, at a streamwise location of $x/h = 12$, in Fig. 16. It can be seen that u_{rms}/U_b increases slightly with increasing Re, however, the values remain between 20 and 22% of the bulk velocity.

Figure 17 shows the cross-flow slices of normalized $\langle uw\rangle$ and $\langle uv\rangle$ components of the Reynolds shear stresses at Re = 9200. Figure 17(a) shows that higher values of $\langle uw\rangle$ appear localized close to the upper and lower walls near the diffuser inlet. However, as flow separates further downstream in Figs. 17(b) and 17(c), we notice that the peak positive $\langle uw\rangle/U_b^2$ contours lie farther away from the wall, indicating the location of the shear layer. The shear layer separates the reverse flow and the peak flow regions, and has a large $\langle uw\rangle$ due to the roll-up of vortices. A comparison with the mean streamwise velocity profiles shown in Fig. 8(a) also confirms that, at a given x/h, the region of high shear that can be inferred from $\partial\langle U\rangle/\partial z$ corresponds to the region with high $\langle uw\rangle$ values. When we compare this with the contours of $\langle uv\rangle$ in Figs. 17(d)–17(f), we notice that the region of high $\langle uv\rangle$ lies toward the side wall (left). The region of high $\langle uv\rangle$ corresponds to the shear layer originating on the face of this wall, which moves farther from the sharp corner as we move in the streamwise direction [Fig. 17(f)]. The $\langle uw\rangle$ and $\langle uv\rangle$ components have their peak values in the shear layers originating from the top and side walls, respectively, both being the diverging walls along which flow separates.

E. Spectral analysis

It was previously shown in the simulations of Malm *et al.* [15], that the separated flow in the upper part of the diffuser (near wall 1) has dominant frequencies which are confined to a narrow low frequency band of St = [0.0092, 0.014]. To investigate this, a frequency analysis of the present time-resolved measurements was carried out for the Re = 9200 case. We use 15 probe locations

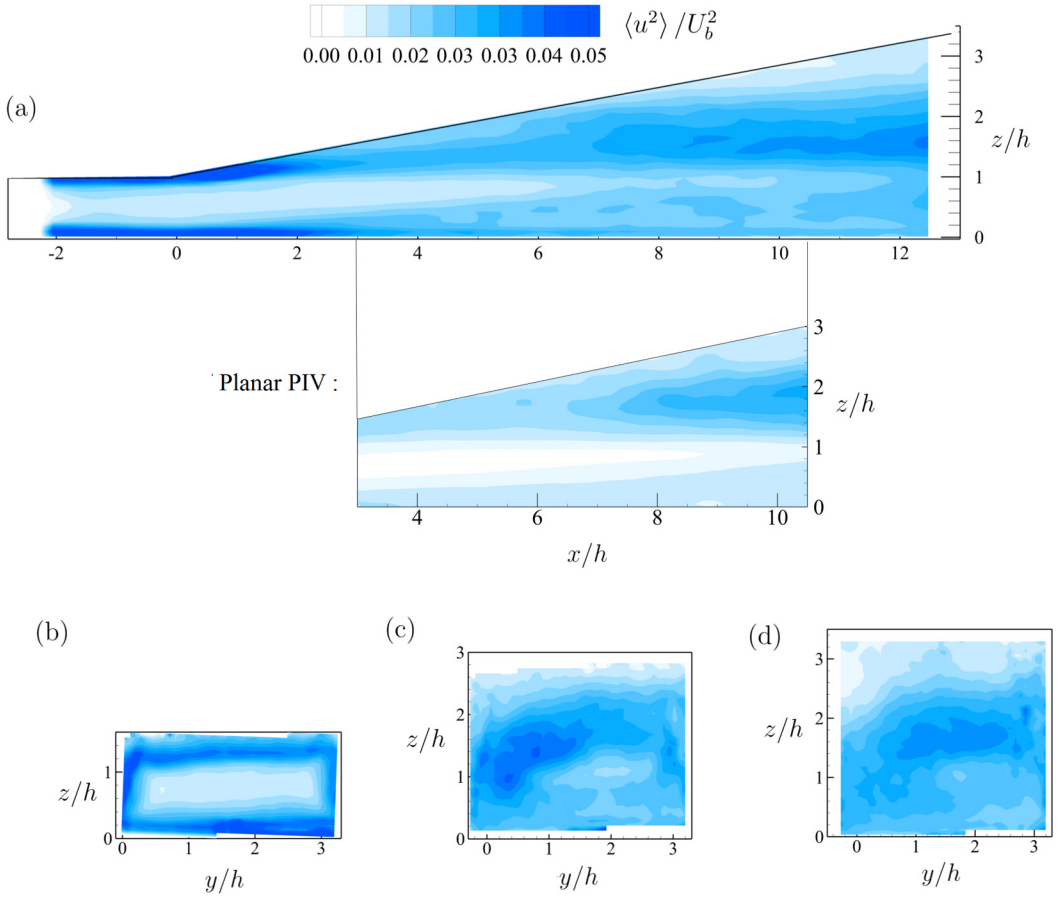

FIG. 15. Reynolds stress contours of $\langle u^2 \rangle / U_b^2$ for Re = 9200. (a) The xz plane at the center plane of $y/h = 1.65$. Also shown in the inset below are the $\langle u^2 \rangle / U_b^2$ contours obtained from planar PIV measurements. The cross-flow slices at three different streamwise locations at $x/h =$ (b) 2, (c) 8, and (d) 12 are also shown.

in the diffuser volume to extract the power spectral density (PSD) of the time signal. These probe locations are at $x/h = 8$, 9, 10, 11, and 12. At each streamwise location, there are three probes located at $y/h = 1$, 1.5, and 2, and at $z/h = 2$. These coordinates are chosen to probe points that surround the separation bubble. PSD is evaluated from instantaneous flow fields over a total duration of $tU_b/h = 613$, with a frequency resolution of St = 0.0027. The PSD of streamwise velocity at each of these points is then averaged and is shown in Fig. 18(a). In addition to this, we also probe six locations in the forward flow region located at $x/h = 7$, 8, 9, 10, 11, and 12, $y/h = 2.1$ and $z/h = 1.1$. The averaged PSD from these probes are shown in Fig. 18(b). Although not shown here, it was verified that each of the individual probes showed similar spectra before they were averaged.

From Fig. 18(a) we note that the dominant frequency peaks near the separated region are observed at the low-frequency range of St = [0.008, 0.02]. Malm *et al.* [15] conjectured that this low-frequency band suggests the presence of self-sustained oscillations in the separated region. In the forward flow region, as shown in Fig. 18(b), we find an additional frequency peak at St = 0.0375. These low-frequency peaks at various locations, both near the separated region and the peak forward-flow regions, indicate that there could be large-scale oscillations present in the flow.

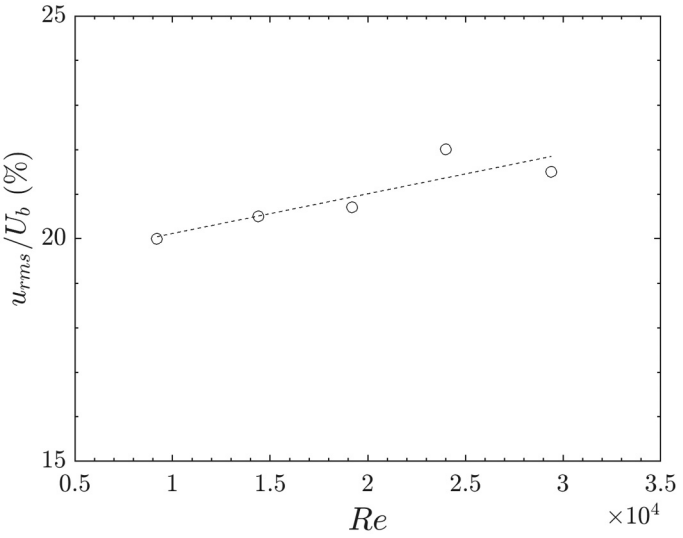

FIG. 16. The peak value of u_{rms}/U_b as a function of Re. The peak value is detected at a streamwise cross section of $x/h = 12$ for all Re. The dotted line is a linear fit to the data.

V. LARGE-SCALE FLOW STRUCTURES

In this section, we present results from the modal decomposition using spectral POD, which in addition to the spatial decomposition, also provides temporal information on large-scale structures in the flow. Next, we present skin-friction lines and their relationship with the 3D topology of the separated flow.

A. Spectral POD

The objective of this analysis is to identify the spatial and temporal characteristics of energy dominant large-scale structures, and to connect them to the dominant frequencies previously identified in Sec. IV E.

The SPOD mode energy as a function of frequency is shown in Fig. 19, where the mode energy is normalized using the total energy. The fraction of total energy in each of the six energy ranked modes is shown in the figure legend. We note that the first mode contains approximately 50% of the total energy, while the last three modes contain only 5.5% of the total energy. To further analyze these, we focus our attention only on the first mode. It can be noted that for the first mode, most of the dominant energy is contained in a low-frequency band near St = 0.01, with two clear identifiable peaks at St = 0.012 and 0.028 marked using dashed lines. These values are similar to the previously noted low-frequency peaks at St = 0.008 and 0.0375 from Fig. 18.

We next look at the spatial organization of the first mode at these identified dominant frequencies. These mode shapes are shown in Fig. 20 at two different frequencies, St = (a) 0.003 and (b) 0.012. The mode shape at the first resolved dominant frequency of St = 0.003 shows two large streamwise streaks which appear to cover the separated regions near walls 1 and 2 in the upper half of the diffuser. The mode shapes oscillating at the dominant frequency of St = 0.012, as shown in Fig. 20(b), appear as streamwise streaks which are aligned closer to wall 2. The presence of these two modes indicates large-scale oscillations at low frequency within the diffuser.

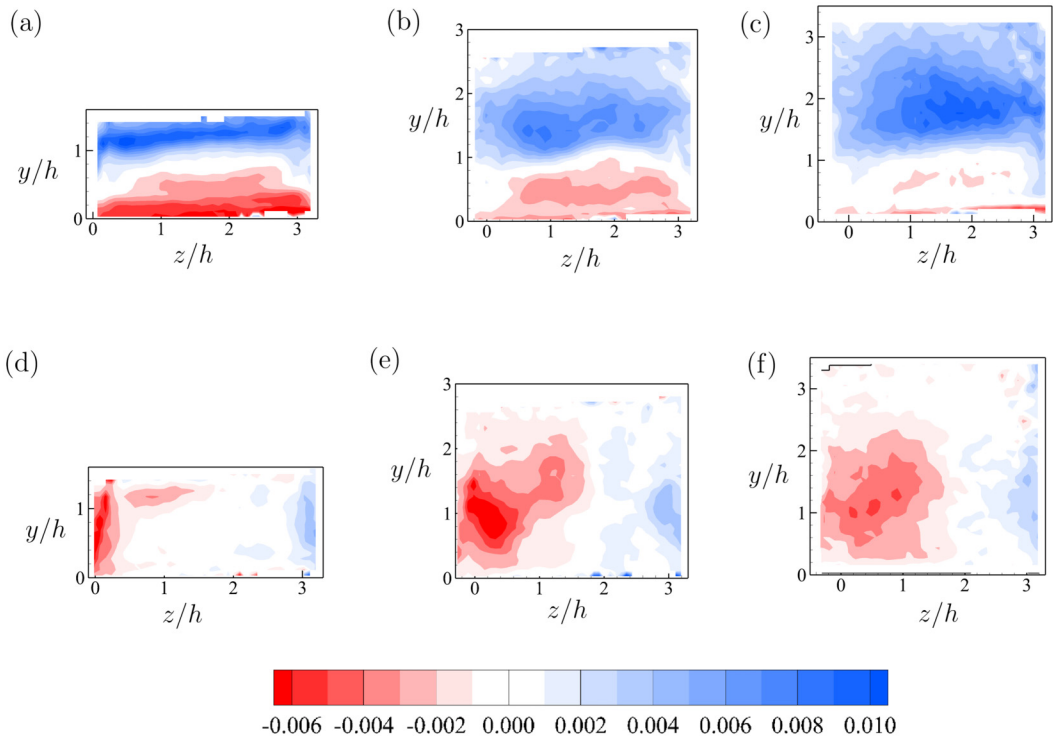

FIG. 17. The contours of $\langle uw \rangle$ and $\langle uv \rangle$ of the Reynolds stress tensor. (a)–(c) $\langle uw \rangle / U_b^2$ contours at $x/h =$ 2, 8, and 12, respectively. (d)–(f) $\langle uv \rangle / U_b^2$ at $x/h = 2$, 8, and 12, respectively. The Re is 9200 in each case.

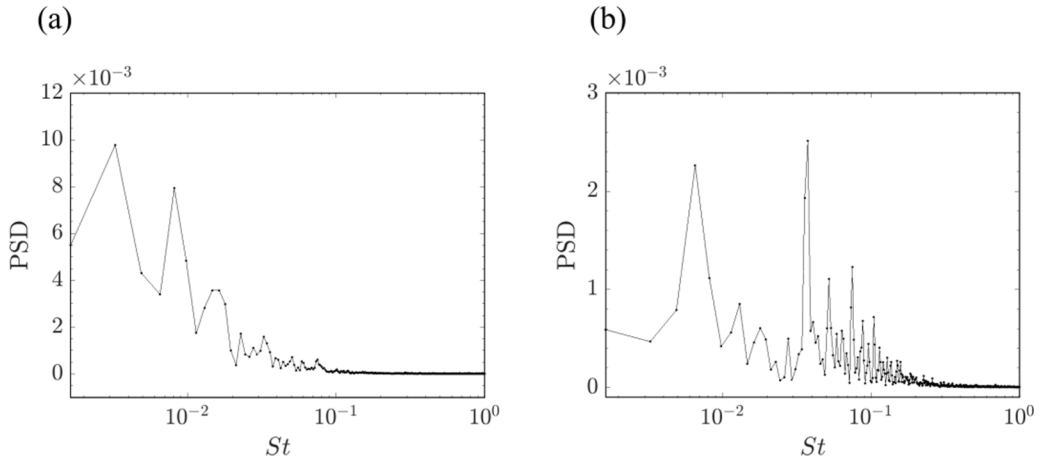

FIG. 18. (a) Averaged PSD plot of 15 probes located at several points in the region bounding the separation bubble. Each streamwise location at $x/h = 8$, 9, 10, 11, and 12 has three probes at $y/h = 1$, 1.5, and 2. The z location of all the probes is at $2h$. (b) Averaged PSD plot of six probes located at $x/h = 7$, 8, 9, 10, 11, and 12, at $y/h = 2.1$ and $z/h = 1.1$. These probe locations are approximately located near the peak forward flow region at each streamwise location.

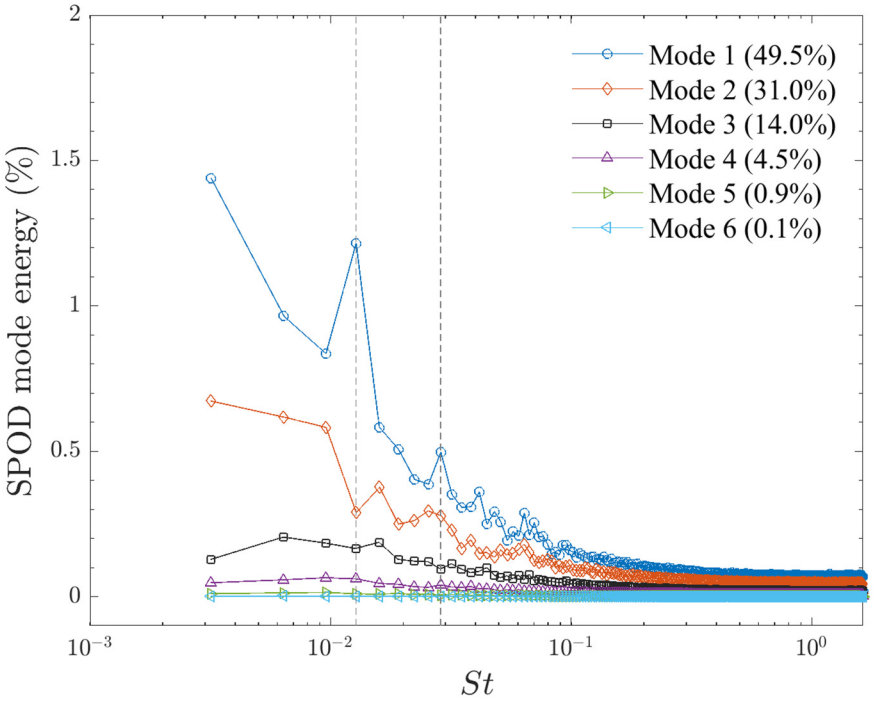

FIG. 19. Mode energy spectrum of different modes normalized with the total energy. The fractional mode energy of each mode is shown in the legend.

B. Skin-friction lines and flow topology

In flow scenarios with 3D separation, the skin-friction lines are used to indicate the separation front. The skin-friction lines in principle should be constructed from vector fields of wall shear stress, where points with zero wall shear stress are the critical points. A classification of various critical points (also referred to as singular points) can be found in the review of Tobak and Peake [47] and in Délery [21]. A necessary condition (defined by Lighthill [48]) for flow separation is when the skin-friction lines converge toward a line originating from a saddle point [47]. Surana *et al*. [49]

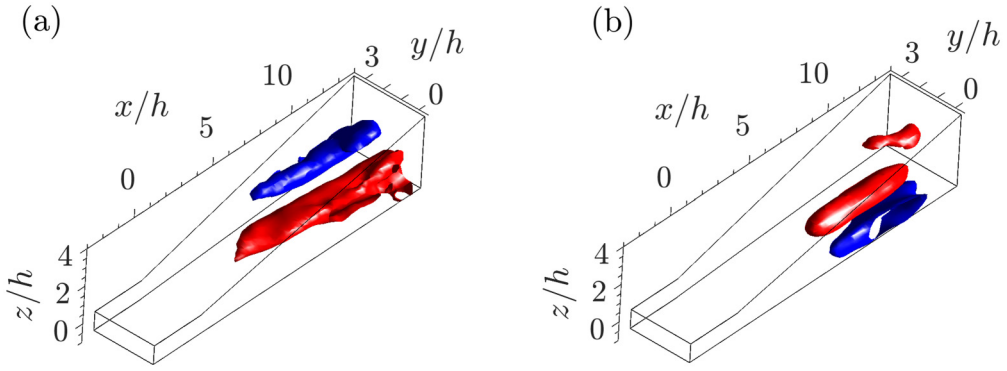

FIG. 20. Spatial organization of mode 1 at Strouhal numbers of (a) 0.003, (b) 0.012. The isosurfaces represent normalized mode magnitude at $\varphi_i = 0.0075$ (blue) and $\varphi_i = -0.0075$ (red).

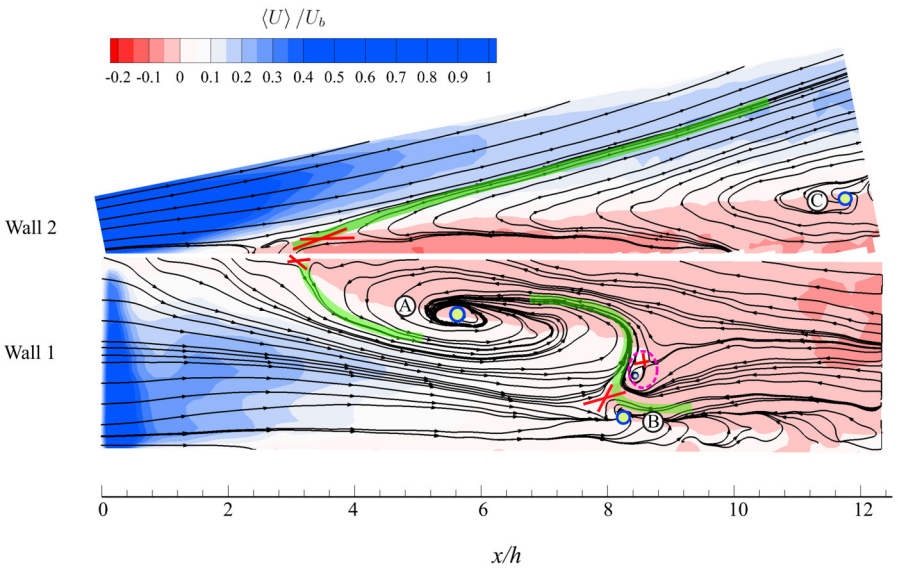

FIG. 21. The streamlines of the mean flow near wall 1 and wall 2 at Re = 9200. Also shown here are the normalized mean streamwise velocity contours.

gave a detailed criteria with theoretical basis on the different conditions when a skin-friction line represents a separation or a reattachment line.

Figure 21 shows the near-wall streamlines of the mean flow which are representative of the topology of the skin-friction lines in the diffuser section. The two walls shown here are wall 1 (top panel) and wall 2 (bottom panel). Although not shown here, we first note that the straight walls on the diffuser do not exhibit any critical points. This is consistent with the observations in Figs. 7 and 10, which show that there is no mean flow separation near these walls, and the streamwise velocities are positive in their vicinity. However, the two diverging walls in Fig. 21 exhibit a rich topology with critical points near the separated flow region. The saddle points are marked with a red cross, and the foci are marked with blue circles. A thick green line is drawn to schematically represent the flow separation line which passes through the saddle points. The most notable structure is a large focus on wall 1 (labeled A) near $x/h = 6$. The other two large scale foci (labeled B and C) appear on wall 1 and wall 2 near $x/h = 8$ and 12, respectively. Two saddle points can be noted near the sharp corner where the two diverging walls meet, at approximately $x/h = 2.8$. Following the notation of Surana *et al.* [49], the separation fronts shown using thick green lines appear to be of the $S1$ type which is defined as a saddle-spiral connection and is one of the four types of possible separation lines. We also note the existence of a saddle-spiral pair on wall 1 near $x/h = 8.5$ encircled using a dotted magenta line. However, this pair does not appear dominant as will be shown later in this section. Overall, we find the presence of four saddle points over both walls, with wall 1 containing three of the saddle points and wall 2 containing one. We also detect four spiral structures (or foci), with there being three on wall 1 and one on wall 2.

It should be noted that the present domain does not include the reattachment region, which in the experiments of Cherry *et al.* [9] was found to occur in the straight section following the diffuser. From the perspective of flow topology, this would suggest the existence of additional critical points in the flow which lie outside of the present measurement domain. This also follows from the flow topology conditions required for the existence of critical points near the reattachment line [49].

To understand how these critical points relate to the flow in the diffuser volume, we next present different cross-sections parallel to diffuser walls 1 and 2 in Fig. 22. The different slices are at a wall-normal distance of (a) 0.2 h, (b) 0.3 h, (c) 0.4 h, and (d) 0.65 h from each of the two diverging

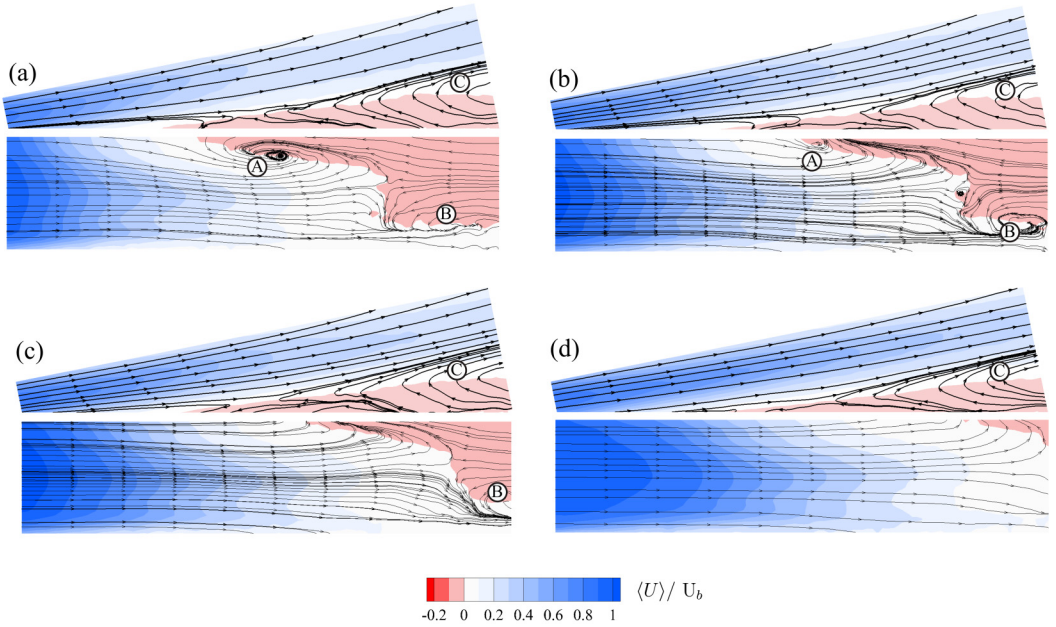

FIG. 22. The in-plane streamlines of the mean velocity at Re = 9200 for planes parallel to wall 2 and wall 1, shown here in the top and bottom sections in each subfigure, respectively. The different planes shown here are at a wall-normal distance of (a) 0.2 h, (b) 0.3 h, (c) 0.4 h, and (d) 0.65 h from their corresponding diverging walls.

walls. As we move away from the wall, the large focus A observed near $x/h = 6$ on wall 1 moves in the streamwise direction and becomes smaller in size. In the cross sections at 0.4 h and 0.65 h from wall 1, this focus can no longer be detected. Similarly, the other large focus B near $x/h = 8$ on wall 1 shifts in the streamwise direction as we move away from the wall, and disappears in Fig. 22(d). The recirculating streamlines on wall 2 (structure C) appear consistently through all the different cross-sections parallel to wall 2. This suggests the wall-normal persistence of a swirling flow region near $x/h = 12$. The saddle-spiral pair near $x/h = 8.5$, which was shown previously in Fig. 21 and was encircled using a dotted magenta line, is detected only on a single cross section in Fig. 22(b), and does not appear to be dominant enough compared to the other structures. Although not shown here, it should be noted that these large scale structures are detected across all Re cases studied and the flow topology for all Re appears qualitatively similar.

A 3D schematic representation of the structures observed is presented in Fig. 23. The separation surface on wall 1 is colored orange and the separation surface on wall 2 is colored cyan. The saddle points on both walls are represented using dotted blue lines. The two dominant spiral structures on wall 1 are shown as conical structures A and B, extruding out from the wall and are connected by an orange separation surface. A saddle point can be noted in between the two structures A and B. The third dominant vortical structure C extrudes out from wall 2 and is connected to the saddle point on wall 2 by a separation surface. The vortical structure A is also connected to another saddle point near the sharp corner formed by the two diverging walls. The separation surface which encloses this saddle-spiral pair also connects to the saddle point near the sharp corner. It can be conjectured that these three separation surfaces, which were also seen in Fig. 21 in the form of thick green lines, would merge and enclose the reverse flow region within the diffuser section. The topology therefore suggests that the flow separates at the sharp corner, and the separated flow extends out on both diverging walls. The backflow region is characterized by three dominant vortical structures, with two of them being on wall 1. These two structures, A and B, slightly extend out from the

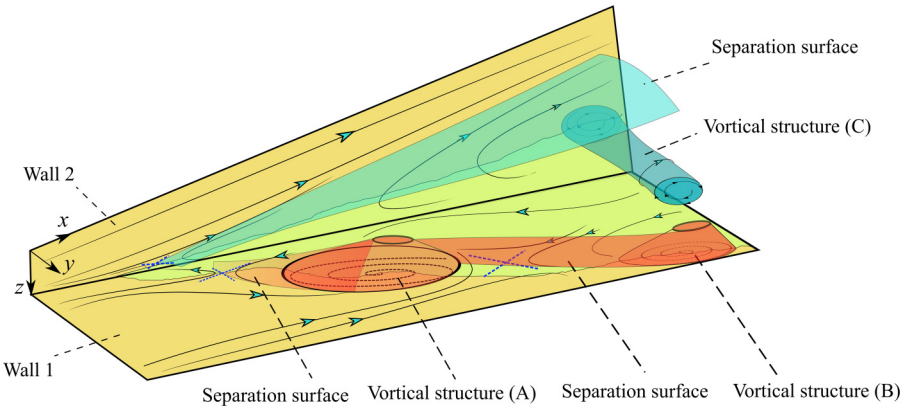

FIG. 23. A 3D schematic of the structures observed in the near-wall regions of the two diverging walls.

wall and then rapidly diminish. However, the structure C from wall 2 extends almost entirely across the width of the diffuser in the y direction. The large spiral structures A–C are seen to be present approximately near the same locations and do not appear visually different in the other Re cases.

VI. CONCLUSIONS

We carried out experiments in a 3D asymmetric diffuser using time-resolved 3D-PTV over a measurement volume of approximately 165 mm $\times$ 35 mm $\times$ 35 mm. The measurements covered the diffuser section, allowing investigation of the 3D flow motions and near-wall streamlines. The state-of-the-art shake-the-box algorithm was used to reconstruct Lagrangian particle tracks, which were then binned in a 3D space to obtain Eulerian 3D flow fields. Experiments were carried out at a total of five different Re ranging from 9200 to 29 400. The diffuser geometry chosen for this study was the diffuser 1 case from Cherry *et al.* [9], which also served as a benchmark case for several numerical studies that followed [11,13–15].

The inlet flow preceding the diffuser section was evaluated using planar PIV. We found that the log-law for the mean velocity profile was satisfied and the Reynolds stresses followed expected trends of a fully developed channel flow. We presented a systematic analysis of the flow in the diffuser section for the Re = 9200 case and showed that the mean flow field was qualitatively similar to those observed in the experiments of Cherry *et al.* [9] and the simulations of Ohlsson *et al.* [11]. Briefly, the flow separation initiated in the sharp corner, where the two diverging walls of the diffuser meet. The separated region then spread over the 11.3° diverging wall as it traversed along the streamwise direction. The streamwise location of the separation point (x_s/h), when observed at a y/h = 1.65 midplane, appeared to move closer to the diffuser inlet with increasing Re. Further analysis also showed that the volume fraction of the backflow region quantified using an intermittency factor (γ), reduced marginally with increasing Re. The Reynolds stress distribution in the diffuser section showed a peak $\langle u^2 \rangle$ in the high shear region separating the back-flow and forward flow regions. The peak u_{rms} values increase marginally with increasing Re, but remain close to approximately 22% of the bulk flow velocity. The in-plane streamlines at a streamwise cross section of the diffuser show the presence of secondary flow well into the diffuser section. The strength of the secondary flows, as quantified by normalized peak vorticity of the secondary vortices, reduced with increasing Re.

A modal decomposition of the fluctuating velocity field was carried out using a SPOD analysis. We identified large-scale structures which were associated with low-frequency oscillations in the range of St = [0.003 0.03]. We found two frequency peaks at St = 0.012 and 0.028, which were associated with the dominant modes. These low-frequency ranges were also noted from a spectral analysis of the flow field by using several probe points bounding the separation bubble.

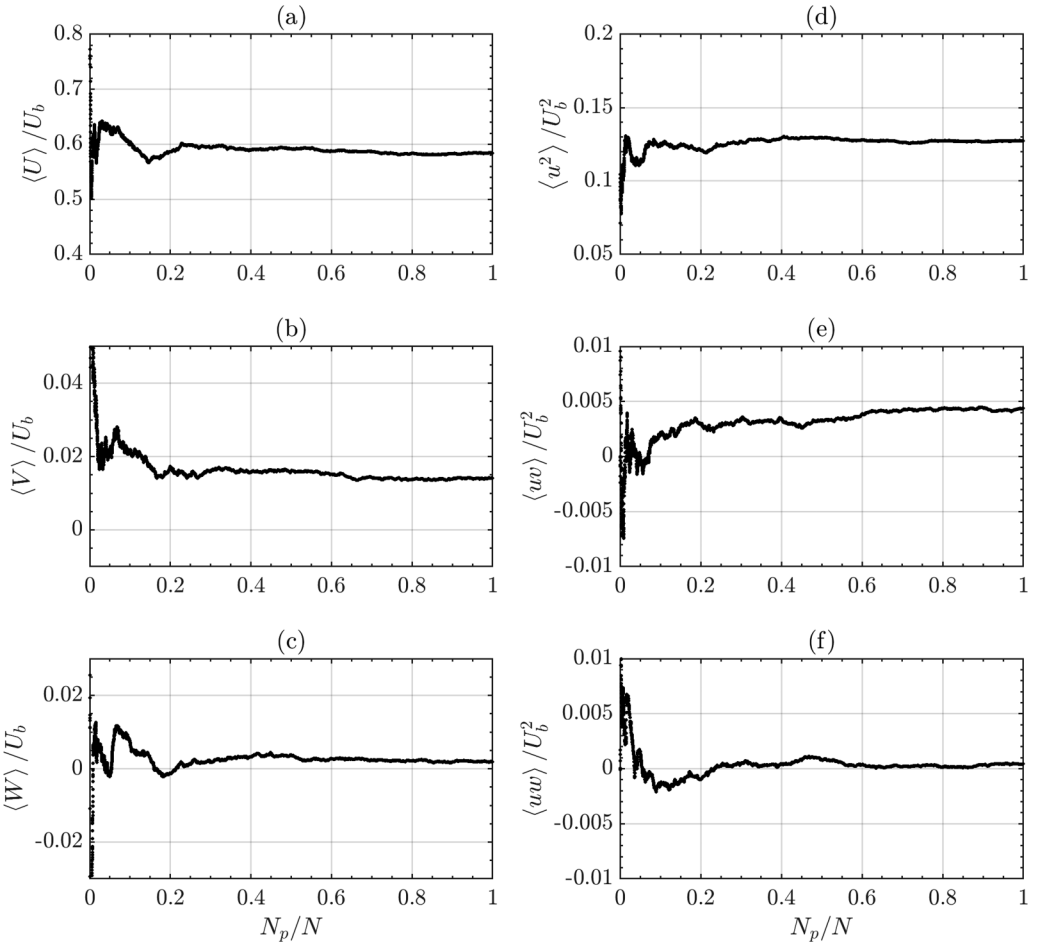

FIG. 24. Statistical convergence of all three components of velocity, and three Reynolds stress components are shown for the Re 9200 case. Each variable is normalized with the bulk flow velocity. The bin size is 5 mm in the streamwise (x) direction and 1.5 mm along the cross-flow (y and z) directions. The center of the bin is located at $x/h = 10$ and y/h, $z/h = 1.6$. The x axis is normalized with the total number of particles (N) in the bin.

The mean flow topology in the diffuser was characterized using near-wall streamlines, showing the existence of critical points near the separation region. Specifically, we detected three saddle points with two on the 11.3° diverging wall (wall 1) and one on the 2.5° diverging wall (wall 2). We also found three large spiral structures, with two on wall 1 (A and B) and one on wall 2 (C). These spiral streamlines were also observed on the planes parallel to the diverging walls, which showed that the spiraling structures extrude out of the walls. These vortical structures were connected via separation surfaces which enclose the backflow region. The foci structures A and B reduced in size with increasing wall-normal distance and rapidly diminished, whereas the structure C emanating from wall 2 extended almost entirely across the width of the diffuser. These overall observations on flow topology were found to be true across all Re cases studied.

ACKNOWLEDGMENTS

The authors acknowledge the financial support of Future Energy Systems at the University of Alberta under Grant No. T15-P05.

APPENDIX

The convergence of velocity and Reynolds stress components measured from 3D-PTV is presented in Fig. 24. The bin size chosen for this statistical convergence is the same that has been used to evaluate all the mean flow analysis in Sec. IV and later. The x axis represents the cumulative number of particles collected in the bin at each time step (N_p) normalized with the total number of particles collected in the bin (N) for the entire acquisition duration. We note that across all the presented quantities, typically the plots converge toward a constant value for $N_p/N > 0.6$. In the cross-flow velocity components [Figs. 24(b) and 24(c)], although the data appears converged, smaller fluctuations remain as they are closer to the uncertainty limits of 0.1 pixel for in-plane component (V) and 0.2 pixels for the out of plane component (W) [34].

[1] R. L. Simpson, Turbulent boundary-layer separation, Annu. Rev. Fluid Mech. **21**, 205 (1989).

[2] R. L. Simpson, Aspects of turbulent boundary-layer separation, Prog. Aerospace Sci. **32**, 457 (1996).

[3] S. Obi, K. Aoki, and S. Masuda, Experimental and computational study of turbulent separating flow in an asymmetric plane diffuser, in Ninth Symposium on "Turbulent Shear Flows" (Kyoto, Japan, 1993).

[4] C. U. Buice and J. K. Eaton, *Experimental investigation of flow through an asymmetric plane diffuser,* Annual Research Briefs (Center for Turbulence Research, Stanford University, 1996), p. 243.

[5] H. J. Kaltenbach, Large-eddy simulation of flow through a plane, asymmetric diffuser, Annual Research Briefs (Center for Turbulence Research, Stanford University, 1994), p. 175–184.

[6] B. F. Armaly, F. Durst, J. C. F. Pereira, and B. Schönung, Experimental and theoretical investigation of backward-facing step flow, J. Fluid Mech. **127**, 473 (1983).

[7] J. Ashjaee and J. P. Johnston, Straight-walled, two-dimensional diffusers—transitory stall and peak pressure recovery, J. Fluids Eng. **102**, 275 (1980).

[8] M. Stieglmeier, C. Tropea, N. Weiser, and W. Nitsche, Experimental investigation of the flow through axisymmetric expansions, J. Fluids Eng. **111**, 464 (1989).

[9] E. M. Cherry, C. J. Elkins, and J. K. Eaton, Geometric sensitivity of three-dimensional separated flows, Int. J. Heat Fluid Flow **29**, 803 (2008).

[10] O. Törnblom, B. Lindgren, and A. V. Johansson, The separating flow in a plane asymmetric diffuser with 8.5° opening angle: Mean flow and turbulence statistics, temporal behavior and flow structures, J. Fluid Mech. **636**, 337 (2009).

[11] J. Ohlsson, P. Schlatter, P. F. Fischer, and D. S. Henningson, Direct numerical simulation of separated flow in a three-dimensional diffuser, J. Fluid Mech. **650**, 307 (2010).

[12] M. Elyasi and S. Ghaemi, Experimental investigation of coherent structures of a three-dimensional separated turbulent boundary layer, J. Fluid Mech. **859**, 1 (2019).

[13] S. Jakirlić, G. Kadavelil, S. Sirbubalo, D. von Terzi, M. Breuer, and D. Borello, SIG15 workshop on refined turbulence modelling, ERCOFTAC Bull. **85**, 5 (2010).

[14] H. Schneider, D. von Terzi, H.-J. Bauer, and W. Rodi, Reliable and accurate prediction of three-dimensional separation in asymmetric diffusers using large-eddy simulation, J. Fluids Eng. **132**, 031101 (2010).

[15] J. Malm, P. Schlatter, and D. S. Henningson, Coherent structures and dominant frequencies in a turbulent three-dimensional diffuser, J. Fluid Mech. **699**, 320 (2012).

[16] S. Grundmann, E. L. Sayles, and J. K. Eaton, Sensitivity of an asymmetric 3D diffuser to plasma-actuator induced inlet condition perturbations, Exp. Fluids **50**, 217 (2011).

[17] S. Grundmann, E. L. Sayles, C. J. Elkins, and J. K. Eaton, Sensitivity of an asymmetric 3D diffuser to vortex-generator induced inlet condition perturbations, Exp. Fluids **52**, 11 (2012).

[18] E. L. Sayles and J. K. Eaton, Sensitivity of an asymmetric, three-dimensional diffuser to inlet condition perturbations, Int. J. Heat Fluid Flow **49**, 100 (2014).

[19] N. Lawson and M. Davidson, Self-sustained oscillation of a submerged jet in a thin rectangular cavity, J. Fluids Structures **15**, 59 (2001).

[20] J. M. Délery, Robert Legendre, and Henri Werlé, Toward the elucidation of three-dimensional separation, Annu. Rev. Fluid Mech. **33**, 129 (2001).
[21] J. Délery, *Three-dimensional Separated Flow Topology.* (John Wiley & Sons, Inc., London, United Kingdom, 2013).
[22] S. Depardon, J. J. Lasserre, J. C. Boueilh, L. E. Brizzi, and J. Borée, Skin friction pattern analysis using near-wall PIV, Exp. Fluids **39**, 805 (2005).
[23] P. Duquesne, Y. Maciel, and C. Deschênes, Unsteady flow separation in a turbine diffuser, Exp. Fluids **56**, 156 (2015).
[24] D. Schanz, A. Schröder, S. Gesemann, D. Michaelis, and B. Wieneke, "Shake The Box": A highly efficient and accurate Tomographic Particle Tracking Velocimetry (TOMO-PTV) method using prediction of particle positions, in *10th International Symposium on Particle Image Velocimetry - PIV13*, Delft, The Netherlands (2010), pp. 1–13.
[25] A. Schröder, D. Schanz, D. Michaelis, C. Cierpka, S. Scharnowski, and C. J. Kähler, Advances of PIV and 4D-PTV "shake the box" for turbulent flow analysis—the flow over periodic hills, Flow, Turbul. Combust. **95**, 193 (2015).
[26] D. Schanz, S. Gesemann, and A. Schröder, Shake-the-box: Lagrangian particle tracking at high particle image densities, Exp. Fluids **57**, 70 (2016).
[27] C. D. Meinhart, S. T. Wereley, and J. G. Santiago, A PIV algorithm for estimating time-averaged velocity fields, J. Fluids Eng. **122**, 285 (2000).
[28] C. J. Kähler, U. Scholz, and J. Ortmanns, Wall-shear-stress and near-wall turbulence measurements up to single pixel resolution by means of long-distance micro-PIV, Exp. Fluids **41**, 327 (2006).
[29] J. Kussin and M. Sommerfeld, Experimental studies on particle behavior and turbulence modification in horizontal channel flow with different wall roughness, Exp. Fluids **33**, 143 (2002).
[30] B. Wieneke, Volume self-calibration for 3d particle image velocimetry, Exp. Fluids **45**, 549 (2008).
[31] D. Schanz, S. Gesemann, A. Schröder, B. Wieneke, and M. Novara, Non-uniform optical transfer functions in particle imaging: Calibration and application to tomographic reconstruction, Meas. Sci. Technol. **24**, 024009 (2012).
[32] G. E. Elsinga, F. Scarano, B. Wieneke, and B. W. van Oudheusden, Tomographic particle image velocimetry, Exp. Fluids **41**, 933 (2006).
[33] See Supplemental Material at https://link.aps.org/supplemental/10.1103/PhysRevFluids.5.114605 for an animation of the Lagrangian particle tracks in time.
[34] W. Abu Rowin and S. Ghaemi, Streamwise and spanwise slip over asuperhydrophobic surface, J. Fluid Mech. **870**, 1127 (2019).
[35] N. Agüera, G. Cafiero, T. Astarita, and S. Discetti, Ensemble 3D PTV for high resolution turbulent statistics, Meas. Sci. Technol. **27**, 124011 (2016).
[36] A. Towne, O. T. Schmidt, and T. Colonius, Spectral proper orthogonal decomposition and its relationship to dynamic mode decomposition and resolvent analysis, J. Fluid Mech. **847**, 821 (2018).
[37] J. L. Lumley, The structure of inhomogeneous turbulence, in *Atmospheric Turbulence and Wave Propagation*, edited by A. M. Yaglom and V. I. Tatarski (Nauka, Moscow, 1967), pp. 166–178.
[38] C. Picard and J. Delville, Pressure velocity coupling in a subsonic round jet, Int. J. Heat Fluid Flow **21**, 359 (2000).
[39] O. T. Schmidt and T. Colonius, Guide to spectral proper orthogonal decomposition, AIAA J. **58**, 1023 (2020).
[40] F. H. Clauser, The Turbulent Boundary Layer, Adv. App. Mech. **4**, 1 (1956).
[41] R. J. Adrian and J. Westerweel, *Particle Image Velocimetry* (Cambridge University Press, New York, 2011).
[42] T. Wei and W. W. Willmarth, Reynolds-number effects on the structure of a turbulent channel flow, J. Fluid Mech. **204**, 57 (1989).
[43] M. Lee and R. D. Moser, Direct numerical simulation of turbulent channel flow up to $Re_\tau \approx 5200$, J. Fluid Mech. **774**, 395 (2015).
[44] R. L. Simpson, A review of some phenomena in turbulent flow separation, J. Fluids Eng. **103**, 520 (1981).
[45] J. P. Johnston, Internal flows, in *Turbulence*, edited by P. Bradshaw (Springer, Berlin, 1976), pp. 109–169.

[46] F. B. Gessner and J. B. Jones, On some aspects of fully-developed turbulent flow in rectangular channels, J. Fluid Mech. **23**, 689 (1965).
[47] M. Tobak and D. J. Peake, Topology of three-dimensional separated flows, Annu. Rev. Fluid Mech. **14**, 61 (1982).
[48] M. J. Lighthill, Attachment and separation in three-dimensional flow, in *Laminar Boundary Layers*, edited by L. Rosenhead (Oxford University Press, London, 1963).
[49] A. Surana, O. Grunberg, and G. Haller, Exact theory of three-dimensional flow separation. Part 1. Steady separation, J. Fluid Mech. **564**, 57 (2006).